The Astrophysical Journal, 976:257 (27pp), 2024 December 1 https://doi.org/10.3847/1538-4357/ad844a

BASS. XLI. The Correlation between Mid-infrared Emission Lines and Active Galactic Nuclei Emission

M. Bierschenk[1], C. Ricci[2,3], M. J. Temple[2], S. Satyapal[1], J. Cann[4,5], Y. Xie[3], Y. Diaz[2], K. Ichikawa[6,7], M. J. Koss[8,9], F. E. Bauer[9,10,11,12], A. Rojas[2,13], D. Kakkad[14], A. Tortosa[15], F. Ricci[16], R. Mushotzky[17,18], T. Kawamuro[19], K. K. Gupta[20,21], B. Trakhtenbrot[22], C. S. Chang[23], R. Riffel[24,25], K. Oh[26], F. Harrison[27], M. Powell[28,29], D. Stern[30], and C. M. Urry[31]

[1] Department of Physics and Astronomy, George Mason University, 4400 University Drive, MSN 3F3, Fairfax, VA 22030, USA
[2] Instituto de Estudios Astrofísicos, Facultad de Ingeniería y Ciencias, Universidad Diego Portales, Avenida Ejercito Libertador 441, Santiago, Chile; claudio.ricci@mail.udp.cl
[3] Kavli Institute for Astronomy and Astrophysics, Peking University, Beijing 100871, People's Republic of China
[4] X-ray Astrophysics Laboratory, NASA Goddard Space Flight Center, Code 662, Greenbelt, MD 20771, USA
[5] Oak Ridge Associated Universities, NASA NPP Program, Oak Ridge, TN 37831, USA
[6] Astronomical Institute, Tohoku University, Aramaki, Aoba-ku, Sendai, Miyagi 980-8578, Japan
[7] Frontier Research Institute for Interdisciplinary Sciences, Tohoku University, Sendai 980-8578, Japan
[8] Eureka Scientific, 2452 Delmer Street, Suite 100, Oakland, CA 94602-3017, USA
[9] Space Science Institute, 4750 Walnut Street, Suite 205, Boulder, CO 80301, USA
[10] Instituto de Astrofísica, Facultad de Física, Pontificia Universidad Católica de Chile, Av. Vicuña Mackenna 4860, Macul Santiago, 7820436, Chile
[11] Centro de Astroingeniería, Facultad de Física, Pontificia Universidad Católica de Chile, Av. Vicuña Mackenna 4860, Macul Santiago, 7820436, Chile
[12] Millennium Institute of Astrophysics, Nuncio Monseñor Sótero Sanz 100, of 104, Providencia, Santiago, Chile
[13] Centro de Astronomía (CITEVA), Universidad de Antofagasta, Avenida Angamos 601, Antofagasta, Chile
[14] Space Telescope Science Institute, 3700 San Martin Drive, Baltimore, MD 21218, USA
[15] INAF—Osservatorio Astronomico di Roma, Via Frascati 33, I-00078 Monte Porzio Catone, Italy
[16] Dipartimento di Matematica e Fisica, Universita Roma Tre, via della Vasca Navale 84, I-00146 Roma, Italy
[17] Department of Astronomy, University of Maryland, College Park, MD 20742, USA
[18] Joint Space-Science Institute, University of Maryland, College Park, MD 20742, USA
[19] RIKEN Cluster for Pioneering Research, 2-1 Hirosawa, Wako, Saitama 351-0198, Japan
[20] STAR Institute, Liège Université, Quartier Agora—Allée du six Août, 19c B-4000 Liège, Belgium
[21] Sterrenkundig Observatorium, Universiteit Gent, Krijgslaan 281 S9, B-9000 Gent, Belgium
[22] School of Physics and Astronomy, Tel Aviv University, Tel Aviv 69978, Israel
[23] Joint ALMA Observatory, Avenida Alonso de Cordova 3107, Vitacura 7630355, Santiago, Chile
[24] Departamento de Astronomia, Instituto de Física, Universidade Federal do Rio Grande do Sul, CP 15051, 91501-970, Porto Alegre, RS, Brazil
[25] Instituto de Astrofísica de Canarias, Calle Vía Láctea s/n, E-38205 La Laguna, Tenerife, Spain
[26] Korea Astronomy & Space Science institute, 776, Daedeokdae-ro, Yuseong-gu, Daejeon 34055, Republic of Korea
[27] Cahill Center for Astronomy and Astrophysics, California Institute of Technology, Pasadena, CA 91125, USA
[28] Kavli Institute for Particle Astrophysics and Cosmology, Stanford University, 452 Lomita Mall, Stanford, CA 94305, USA
[29] Department of Physics, Stanford University, 382 Via Pueblo Mall, Stanford, CA 94305, USA
[30] Jet Propulsion Laboratory, California Institute of Technology, 4800 Oak Grove Drive, MS 169-224, Pasadena, CA 91109, USA
[31] Yale Center for Astronomy & Astrophysics, Physics Department, PO Box 208120, New Haven, CT 06520-8120, USA

Received 2023 November 15; revised 2024 September 16; accepted 2024 September 16; published 2024 November 27

Abstract

We analyze Spitzer spectra of 140 active galactic nuclei (AGN) detected in the hard X-rays (14–195 keV) by the Burst Alert Telescope on board Swift. This sample allows us to probe several orders of magnitude in black hole masses (10^6–$10^9 M_\odot$), Eddington ratios (10^{-3}–1), X-ray luminosities (10^{42}–10^{45} erg s^{-1}), and X-ray column densities (10^{20}–10^{24} cm^{-2}). The AGN emission is expected to be the dominant source of ionizing photons with energies $\gtrsim$50 eV, and therefore, high-ionization mid-infrared (MIR) emission lines such as [Ne V] 14.32, 24.32 μm and [O IV] 25.89 μm are predicted to be good proxies of AGN activity, and robust against obscuration effects. We find high detection rates ($\gtrsim$85%–90%) for the MIR coronal emission lines in our AGN sample. The luminosities of these lines are correlated with the 14–150 keV luminosity (with a typical scatter of $\sigma \sim$0.4–0.5 dex), strongly indicating that the MIR coronal line (CL) emission is driven by AGN activity. CLs are also tightly correlated to the bolometric luminosity ($\sigma \sim$0.2–0.3 dex), calculated from careful analysis of the spectral energy distribution. We find that the relationship between the CL strengths and $L_{14-150\,\mathrm{keV}}$ is independent of black hole mass, AGN luminosity, and Eddington ratio, and mostly not affected by high X-ray column densities. This confirms that the MIR CLs can be used as unbiased tracers of the AGN power for X-ray luminosities in the 10^{42}–10^{45} erg s^{-1} range.

Unified Astronomy Thesaurus concepts: Active galactic nuclei (16); Galaxy nuclei (609); High energy astrophysics (739)

1. Introduction

It is well established that supermassive black holes (SMBHs) lie at the center of most massive galaxies and that they could play an important role in the evolution of their host galaxy (e.g., J. Kormendy & D. Richstone 1995; J. Magorrian et al.

1998; K. Gebhardt et al. 2000; J. Kormendy & L. C. Ho 2013). SMBHs can grow by accreting gas and dust from their host galaxies. These accreting SMBHs, or active galactic nuclei (AGN), are some of the brightest objects in the Universe, emitting large amounts of radiation across the entire electromagnetic spectrum (e.g., M. Elvis et al. 1994; L. C. Ho 2008; J. R. Mullaney et al. 2011). Some of the most luminous AGN have been found to have bolometric luminosities up to 10^{48} erg s^{-1} (e.g., R. J. Assef et al. 2015; T. Díaz-Santos et al. 2016; M. Bischetti et al. 2017; S. Martocchia et al. 2017; L. Zappacosta et al. 2020). Surrounding the SMBH and its accretion flow is a parsec-scale anisotropic structure of gas and dust, often referred to as the torus, which absorbs and reprocesses the radiation from the accretion disk (e.g., R. Antonucci 1993; C. M. Urry & P. Padovani 1995; H. Netzer 2015; C. R. Almeida & C. Ricci 2017). According to the simplest AGN unification model (e.g., R. Antonucci 1993), depending on the viewing angle with respect to the obscuring material, light from the AGN can suffer from strong extinction. About 70% of the AGN in the local Universe are obscured by gas with column densities $N_{\rm H} \geqslant 10^{22}$ cm^{-2} (e.g., C. Ricci et al. 2015, 2017b), and a significant fraction (∼20%–30%) of them are obscured by Compton-thick material ($N_{\rm H} \geqslant 10^{24}$ cm^{-2}; D. Burlon et al. 2011; C. Ricci et al. 2015; N. Torres-Albà et al. 2021; A. Tanimoto et al. 2022).

One of the best ways to identify AGN is to select them in the hard X-ray band (>10 keV), where contamination from the host galaxy is negligible. Hard X-rays are also not strongly affected by obscuration, at least up to $N_{\rm H} \sim 10^{24}$ cm^{-2} (e.g., C. Ricci et al. 2015), and therefore, they can provide an almost unbiased sample of AGN in the local universe. However, hard X-rays can be attenuated for $N_{\rm H} \gtrsim 10^{24}$ cm^{-2}, so the most heavily obscured AGN can be easily missed by hard X-ray surveys (C. Ricci et al. 2015). Obscured AGN can also be identified using optical emission line ratios (e.g., J. A. Baldwin et al. 1981; S. Veilleux & D. E. Osterbrock 1987; L. J. Kewley et al. 2001; G. Kauffmann et al. 2003), although it is important to stress that a significant fraction of hard X-ray selected AGN may not be classified as AGN by optical emission line spectroscopy due to contamination from star formation or merger-associated dust obscuration (e.g., C. Ricci et al. 2017a; M. J. Koss et al. 2018; C. Ricci et al. 2021; S. Yamada et al. 2021).

Another method to identify AGN is via the detection of forbidden emission lines with ionization potentials (IPs) $\gtrsim$54 eV (i.e., the double ionization edge of helium), commonly referred to as "coronal lines" (CLs). In AGN, the CLs are emitted in the so-called CL region, likely located in the narrow-line region and beyond the broad-line region (e.g., J. Negus et al. 2023). The presence of CLs can serve as an important indicator of AGN activity, as they are extremely difficult to produce through stellar processes and are more likely created by AGN photoionization (e.g., E. Sturm et al. 2002; S. Satyapal et al. 2007; N. P. Abel & S. Satyapal 2008; S. Satyapal et al. 2008; A. D. Goulding & D. M. Alexander 2009; S. Satyapal et al. 2009; M. Pereira-Santaella et al. 2010; C. Gruppioni et al. 2016; J. M. Cann et al. 2018; N. Maddox 2018; L. Spinoglio et al. 2022; A. Feltre et al. 2023; L. Hermosa Muñoz et al. 2024; J. D. McKaig et al. 2024; L. Zhang et al. 2024). However, some authors have suggested that CL emission could also be enhanced by shocks, driven by the interaction of a radio jet and the interstellar medium, by outflowing material or associated with mergers (e.g., Y. I. Izotov et al. 2012; X. Mazzalay et al. 2013; A. Rodríguez-Ardila et al. 2017; A. Rodríguez-Ardila & M. A. Fonseca-Faria 2020; F. C. Cerqueira-Campos et al. 2021; M. A. Fonseca-Faria et al. 2021; J. Negus et al. 2021; F. C. Cerqueira-Campos et al. 2023). With the recent launch of the James Webb Space Telescope (JWST; J. P. Gardner et al. 2006), CLs have gained significant relevance. Now is an ideal time to revisit the use of infrared CLs as proxies of AGN activity, and to refine our understanding of how CL emission varies across the broader AGN population.

Constraining the bolometric luminosity of an AGN is crucial to understanding the energetics of such systems and to infer their accretion rates. Since most AGN are obscured (with no direct constraints on the dominant UV emission), estimating their intrinsic luminosity can be complicated. Several empirical relations linking X-ray luminosities to optical lines (e.g., L. Bassani et al. 1999), mid-infrared (MIR) continuum (P. Gandhi et al. 2009; D. Asmus et al. 2015), and more recently, the nuclear 100 GHz (C. Ricci et al. 2023) and 200 GHz (T. Kawamuro et al. 2022, 2023) millimeter continuum luminosities, have been used for this purpose. L. Bassani et al. (1999) showed that the luminosity of [O III] 5007 Å is correlated with X-ray luminosity (see also S. Berney et al. 2015; Y. Ueda et al. 2015; K. Oh et al. 2017, 2022), albeit with a large (∼0.6–0.7 dex) scatter. Some of these correlations with photoionized optical lines can, in fact, be strongly affected by obscuration, AGN variability, contamination from stellar sources, and biased samples, which would greatly enhance their scatter. Near-infrared (NIR) CLs of hard X-ray selected AGN (e.g., [Si VI] 1.96 μm) have been shown to be significantly more tightly correlated to the X-ray luminosity (with a scatter of 0.37 dex) than the optical [O III] λ 5007 line (0.71 dex), possibly due to obscuration or the higher ionization required (e.g., I. Lamperti et al. 2017; J. S. den Brok et al. 2022).

The MIR is an ideal wave band to probe AGN activity in obscured systems, due to the relatively low effect of dust attenuation (e.g., D. W. Weedman et al. 2005; L. Armus et al. 2006; A. D. Goulding & D. M. Alexander 2009). P. Gandhi et al. (2009; see also D. Asmus et al. 2015) found that the nuclear MIR luminosities of AGN are strongly correlated to their X-ray luminosities. However, high-resolution (HR) observations are needed to mitigate the influence of the host galaxy, particularly for low-luminosity AGN. In the MIR, there are several forbidden lines that could be used as tracers of AGN activity. Examples of these lines are [Ne V] 14.32 and 24.32 μm (e.g., S. Satyapal et al. 2007, 2008), [O IV] 25.89 μm (e.g., M. Meléndez et al. 2008), and [S III] 18.71 and 33.48 μm which have ionization energies of 97, 55 and 24 eV respectively (see Table 1 in S. Satyapal et al. 2021 for a list of CL ionization energies). Therefore, these high-ionization MIR emission lines have the potential to be good proxies of the intrinsic luminosity of AGN, even in obscured systems where it can be particularly complicated to estimate the AGN power (e.g., R. C. Hickox & D. M. Alexander 2018). It should be mentioned, however, that this might not be the case for AGN in galaxies undergoing the final stages of a merger, where [Ne V] and [O IV] have been found to be weak (S. Yamada et al. 2024), likely because of the very large covering factor of the obscuring material (C. Ricci et al. 2017a, 2021; S. Yamada et al. 2024).

In this work, we present the largest study to date of MIR coronal emission lines for a sample of hard X-ray selected AGN to test whether they can be used as proxies of AGN activity. We carefully analyzed the MIR spectra of 140 sources using Spitzer/Infrared Spectrograph (IRS) data. Our sample is selected by crossmatching the ∼860 sources of the Swift/BAT AGN Spectroscopic Survey (BASS[32]) with the Spitzer archive. The BASS sample contains a wealth of multiwavelength ancillary data and derived properties (e.g., SMBH mass, accretion rate, and column density; M. Koss et al. 2017; C. Ricci et al. 2017b; M. J. Koss et al. 2022a; J. E. Mejía-Restrepo et al. 2022), which allows us to test the dependence of CL fluxes on AGN properties, expanding previous studies of smaller samples (e.g., M. Meléndez et al. 2008; S. Tommasin et al. 2008; S. Tommasin et al. 2010; K. A. Weaver et al. 2010; C. Gruppioni et al. 2016; L. Spinoglio et al. 2022; A. Feltre et al. 2023). The structure of the paper is as follows. Our sample, the Spitzer/IRS, and the multiwavelength data we use are presented in Section 2. The fitting methods for determining the fluxes of the forbidden emission lines [Ne V] 14.32/24.32 μm, [O IV] 25.89 μm, and [S III] 18.71/33.48 μm are provided in Section 3. Our analysis is described in Section 4, while Section 5 is dedicated to results and discussion. Throughout this work, we assume the following standard cosmological parameters: $H_0 = 71$ km s^{-1} Mpc^{-1}, $\Omega_m = 0.30$, and $\Omega_\Lambda = 0.70$.

2. Sample and Data

2.1. BASS Sample: Data and Derived Properties

To test the effectiveness of high-ionization emission lines as a proxy for AGN activity, we use the sample of AGN detected in the 14–195 keV band by the Burst Alert Telescope (BAT; S. D. Barthelmy et al. 2005) on board the Neil Gehrels Swift Observatory (N. Gehrels et al. 2004) during its first 70 months of operations (W. H. Baumgartner et al. 2013). This sample is highly complete, being almost unbiased by obscuration up to $N_{\rm H} \sim 10^{24}$ cm^{-2} (e.g., C. Ricci et al. 2015). The sample also has a large amount of multiwavelength data available, which includes data in the X-rays (C. Ricci et al. 2017b), optical (M. Koss et al. 2017, 2022b; J. E. Mejía-Restrepo et al. 2022), infrared (I. Lamperti et al. 2017; K. Ichikawa et al. 2017, 2019; J. S. den Brok et al. 2022; F. Ricci et al. 2022b), millimeter (M. J. Koss et al. 2021; T. Kawamuro et al. 2022; C. Ricci et al. 2023) and radio (J. Baek et al. 2019; K. L. Smith et al. 2020). This large effort has led to several studies comparing the optical and X-ray properties of AGN with their black hole masses and accretion rates (K. Oh et al. 2017; C. Ricci et al. 2017c, 2018, 2022a, 2022b; B. Trakhtenbrot et al. 2017; A. F. Rojas et al. 2020; D. Kakkad et al. 2022).

The X-ray properties (i.e., intrinsic X-ray luminosities and column densities) for all AGN in the BASS sample were taken from the dedicated X-ray spectroscopic analysis of the AGN from the flux-limited 70 month Swift/BAT catalog (C. Ricci et al. 2017b), while the black hole masses for 780 of these objects were taken from the second BASS data release (M. J. Koss et al. 2022b). black hole masses ($M_{\rm BH}$) in BASS have been determined using different approaches, such as the virial method using the Hα and Hβ lines (e.g., Y. Shen 2013) and the $M_{\rm BH}$–σ_* relation (e.g., J. Kormendy & L. C. Ho 2013). For unobscured AGN, BASS uses masses derived from broad Hα and Hβ lines. For obscured sources, BASS considers black hole masses inferred from velocity dispersion measurements (M. J. Koss et al. 2022c), since in these objects, the broad Hα and Hβ lines can be significantly affected by obscuration, leading to an underestimation of $M_{\rm BH}$ (e.g., J. E. Mejía-Restrepo et al. 2022; F. Ricci et al. 2022b). The large multiwavelength coverage of BASS sources allows us to have well-determined measurements of AGN properties such as black hole mass ($M_{\rm BH}$), Eddington ratio ($\lambda_{\rm Edd} = L_{\rm bol}/L_{\rm Edd}$), intrinsic X-ray luminosity ($L_{14-150\,{\rm keV}}$), and line-of-sight column density ($N_{\rm H}$). The bolometric luminosities were calculated using a uniform bolometric correction in the 14–150 keV band ($\kappa_{14-150} = 8.48$), which is equivalent to a 2–10 keV bolometric correction of $\kappa_{2-10} = 20$ (R. V. Vasudevan & A. C. Fabian 2009) for $\Gamma = 1.8$, the median photon index of nearby AGN (C. Ricci et al. 2017b). However, in Section 4.2, we also consider recently calculated bolometric corrections for most of the unobscured AGN in our sample, using the recent results of K. K. Gupta et al. (2024).

2.2. Spitzer/IRS Spectral Data

To measure the MIR emission line properties, we use archival spectra from the IRS on board the Spitzer Space Telescope. Spitzer/IRS spectra were downloaded from the HR1 version of the Combined Atlas of Sources with Spitzer IRS Spectra (CASSIS; V. Lebouteiller et al. 2015), available online.[33] We use the HR $R \sim 600$ spectra (measuring emission on 5″–20″ angular scales; see Table 3 of V. Lebouteiller et al. 2015), which typically cover the 10−38 μm range.[34] This is sufficient to separate commonly blended emission features such as [O IV] and [Fe II] at 25.89 and 26.00 μm, respectively, and [Ne V] and [Cl II] at 14.32 and 14.37 μm. Our final sample was obtained by crossmatching the BASS and CASSIS samples, resulting in 140 objects with median $\log(N_{\rm H}\ {\rm cm}^{-2}) = 22.12$, $\log(M_{\rm BH}/M_\odot) = 7.68$, $\log \lambda_{\rm Edd} = -1.46$, and $\log(L_{14-150\,{\rm keV}}\ {\rm erg\ s}^{-1}) = 43.34$. In Figure 1, we show the distributions of column density (top left panel), black hole mass (top right panel), 14–150 keV luminosity (bottom left panel), and Eddington ratio (bottom right panel) for the whole BASS sample (dark colors) and for our subsample of AGN with Spitzer/IRS spectra available. A Kolmogorov–Smirnov test shows that the Spitzer/IRS sample studied here is broadly representative of the wider BASS sample, although it preferentially selects lower luminosity AGN. This is also clearly shown in Figure 2, and is associated with the typically lower redshifts ($z \lesssim 0.1$) of AGN with Spitzer/IRS observations. About half of the objects of our sample have been studied in K. A. Weaver et al. (2010), and in Appendix D, we report a comparison with their study.

3. Spitzer/IRS Spectral Analysis

3.1. Line Fitting

To measure the MIR emission line fluxes, we used the PYTHON LMFIT package (M. Newville et al. 2014) to model the emission lines in the Spitzer spectra. Our model includes a power law for the continuum (spanning across ±0.12 μm for [Ne V] 14.32 μm, ±0.15 μm for [S III] 18.71 μm, ±0.22 μm

---

[32] https://www.bass-survey.com/

[33] https://cassis.sirtf.com/

[34] One source had a spectrum covering only the 9–18 μm range (SDSS J130005.35+163214.8; see Appendix A).

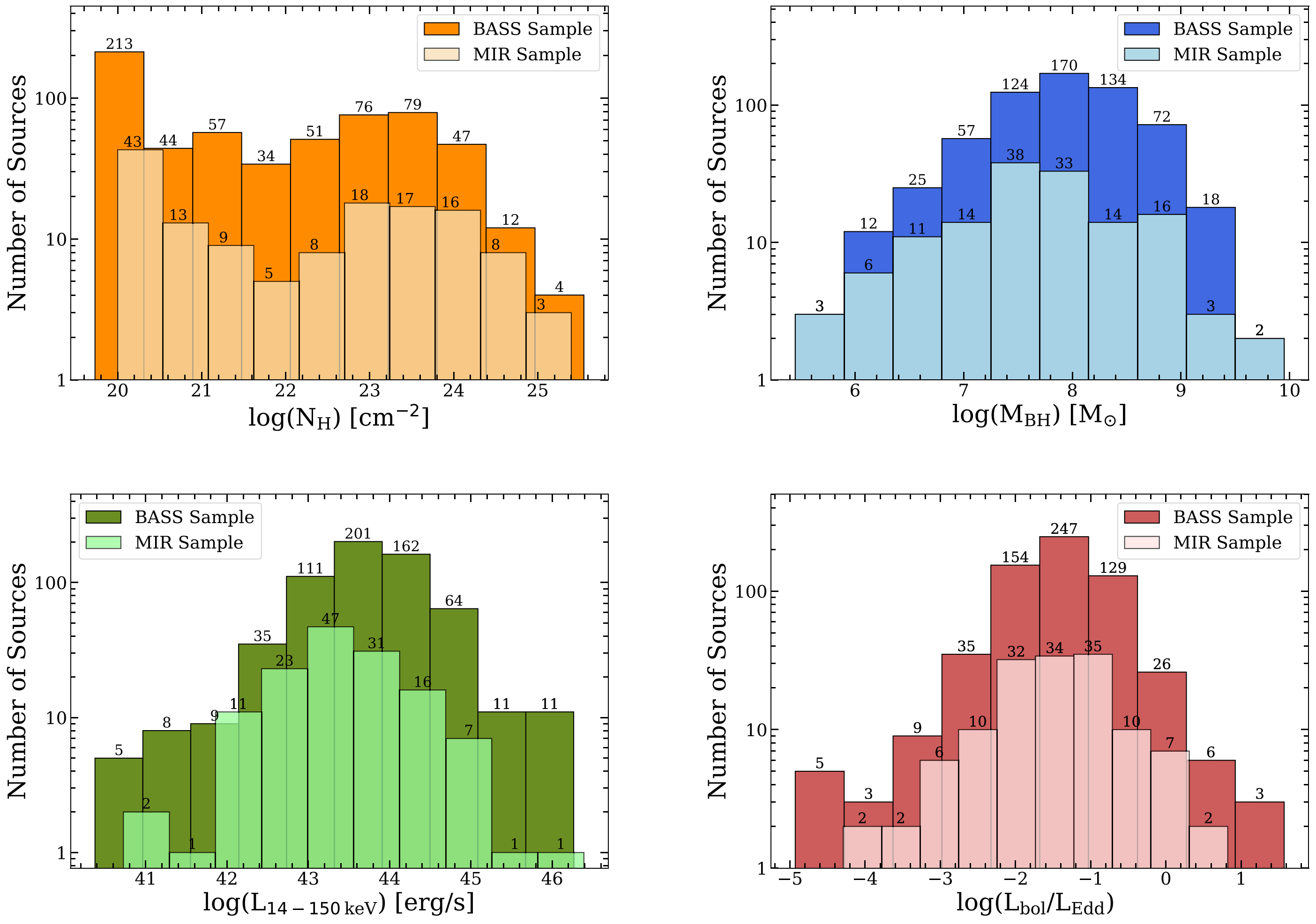

Figure 1. The number of sources as a function of obscuring column density [$\log(N_H)$], black hole mass [$\log(M_{BH})$], intrinsic 14–150 keV X-ray luminosity [$\log(L_{14-150\text{ keV}})$], and Eddington ratio ($\log(\lambda_{Edd})$] for the parent BASS sample (darker shades) and the sample with MIR spectra used in this work (lighter shades).

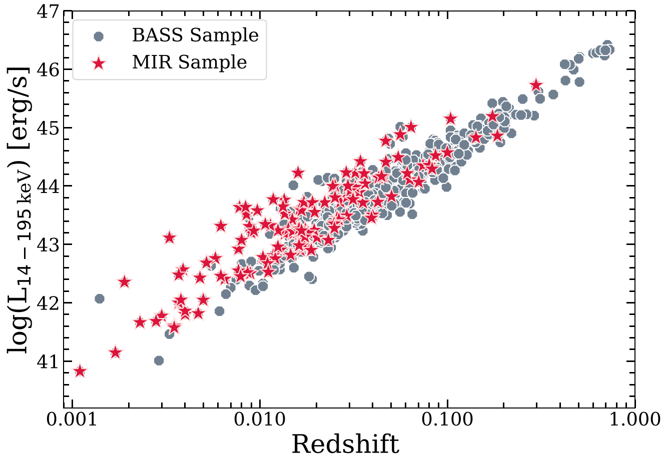

Figure 2. The 14–195 keV X-ray luminosities as a function of redshift for the sample with MIR spectroscopy used in this work (red stars) compared to the complete BAT-selected sample (gray points). The majority of the objects with Spitzer/IRS spectra have $z < 0.1$, and span nearly the full range of luminosities seen in the wider BASS population.

for [Ne V] 24.32 μm, $\pm 0.25\,\mu$m for [O IV] 25.89 μm, and $\pm 0.25\,\mu$m for [S III] 33.48 μm) and Gaussian lines for each emission feature. For each line, we set the centroid wavelength to the rest-frame wavelength of the emission line with an uncertainty range of $\pm\lambda$/spectral resolution $= \pm\lambda/600$, allowing the line amplitude, continuum parameters, and sigma to vary. The latter parameter was allowed to vary within the range of $\pm 3\lambda/600/2.36$. In most cases, the best-fit centroid wavelength was consistent with the expected value (see Appendix C). This model was applied to five emission lines: [Ne V] 14.32/24.32 μm, [S III] 18.71/33.48 μm, and [O IV] 25.89 μm. To determine the error on the flux, we applied a bootstrapping method to generate, for every source and each MIR emission line, 100 simulated spectra by considering the errors on each individual wavelength bin, and then obtained the flux and corresponding continuum parameters from each individual simulated spectra. The standard deviation of the 100 fluxes was used as the uncertainty on the reported flux. An example fit of a clear detection (a detection being when the signal-to-noise ratio (S/N) was greater than or equal to 3.0, i.e., S/N $\geqslant 3$) of [Ne V] 14.32 μm is presented in the top left panel of Figure 3.

Given the limited ($R \approx 600 \approx 500$ km s^{-1}) resolution of Spitzer/IRS, the CLs studied in this work are essentially unresolved in the vast majority of objects in our sample. However, while most lines were well-described by a single Gaussian (between ∼55% and ∼90%, see Table 1), in some cases, a multicomponent decomposition of up to three Gaussians was required to adequately model the data (see Section 3.3.4 and bottom right panel of Figure 3). For each

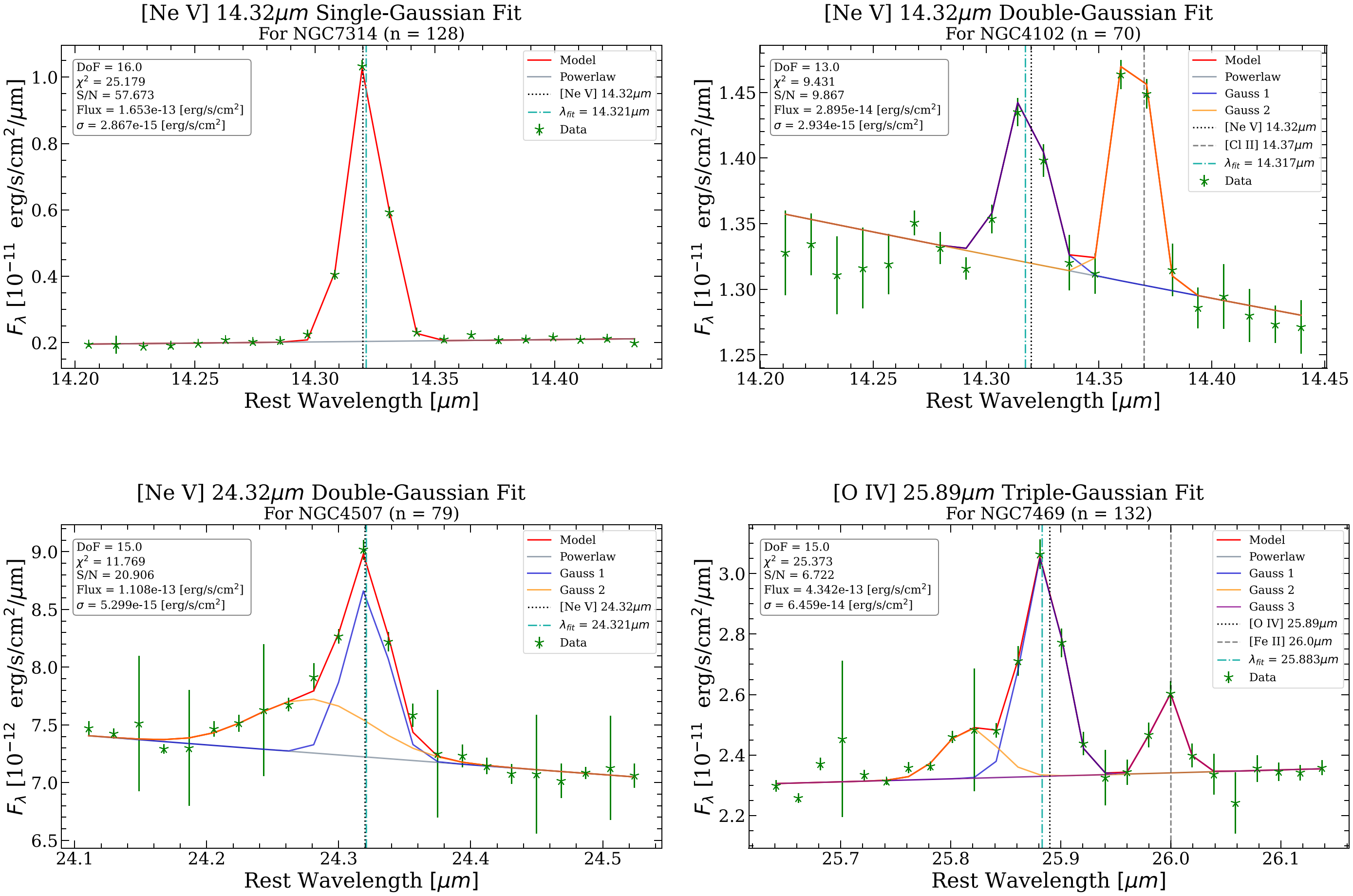

Figure 3. Examples of fits and special cases. Top left panel: single-Gaussian plus a power-law model for the [Ne V] emission line at 14.32 μm in the IR spectrum of NGC 7314; see Section 3.1. Top right panel: double-Gaussian plus a power-law model for the [Ne V] emission at 14.32 μm in the IR spectrum of NGC 4102. This model included the nearby [Cl II] 14.37 μm line. The reported flux for this source is that of the first Gaussian curve only (blue line); see Section 3.3.1. Bottom left panel: double-Gaussian plus a power-law model for the [Ne V] emission at 24.32 μm in the IR spectrum of NGC 4507. These spectra had a blueshifted velocity peak, which may suggest the presence of outflows. In such cases we also consider the flux of the second Gaussian, thus, the total flux (red line) for this line is the sum of the fluxes of both Gaussians; see Section 3.3.2. Bottom right panel: triple-Gaussian plus a power-law model for the [O IV] emission at 25.89 μm in the IR spectrum of NGC 7469. This spectrum included a blueshifted velocity peak as well as emission at longer wavelengths. In this case, we adopt a similar method as for the blue excess by considering the fluxes of the first and second Gaussian lines as the total flux of the emission line (blue line + orange line). The reported flux determination varies depending on the specific case; see Section 3.3.4.

Table 1
Fit Statistics

Emission line	Fit Total	Detections	Upper Limits	Single	Double				Triple			
				Tot	Tot	O	R	B	Tot	O+R	O+B	B+R
(1)	(2)	(3)	(4)	(5)	(6)	(7)	(8)	(9)	(10)	(11)	(12)	(13)
[Ne V] 14.32 μm	140	123 (88%)	17 (12%)	105	17	4	8	5	1	1	0	0
[S III] 18.71 μm	136	128 (94%)	8 (6%)	121	7	4	0	3	N/A	…	…	…
[Ne V] 24.32 μm	139	118 (85%)	21 (15%)	109	9	6	0	3	N/A	…	…	…
[O IV] 25.89 μm	139	135 (96%)	4 (3%)	77	50	2	43	5	8	5	1	2
[S III] 33.48 μm	131	120 (92%)	11 (8%)	118	2	1	0	1	N/A	…	…	…

Note. Breakdown of the different models required to fit the spectra for each CL. The columns include the following information:
(1) List of the five forbidden emission lines studied here. (2) Total number of spectra fitted for each line. Although we started with a full sample of 140 sources, for various reasons, the spectra of some sources could not be used. This is explained in detail in Appendix A. (3) Number of detections for each emission line described in Section 3.1. (4) Number of nondetections/upper limits described in Section 3.2. (5) Number of objects that only required a single Gaussian. (6–9) Number of sources that needed two Gaussian lines. (7) Sources for which the second Gaussian accounts for a blueshifted line, which could be an outflow signature ("O"), described in Section 3.3.2. We use "O" to distinguish these objects from those showing "broad" lines; see Section 3.3.3. (8) AGN in which a second Gaussian was included to take into account a nearby emission line at longer (redder) wavelengths ("R"). These components describe the fitting accommodation of [Cl II] 14.37 μm and [Fe II] 26.0 μm, for [Ne V] 14.32 μm and [O IV] 25.89 μm, respectively; see Section 3.3.1. (9) Sources that required an additional broad Gaussian line centered at the same wavelength as the expected emission line ("B"), described in Section 3.3.3. (10–13) Number of objects that required two additional Gaussian lines to fit the spectra. (11) Sources showing a blueshifted line as well as a nearby emission line on the red side ("O+R"); see Section 3.3.4. (12) Objects showing blueshifted lines and one broad component ("O+B"); see Section 3.3.4. (13) AGN that needed one broad line and one nearby emission line on the red side ("B+R"); see Section 3.3.4.

object, we start with the simplest model of a single Gaussian, then progress to more complex models by adding additional Gaussian components, depending on how much the reduced χ^2 value deviates from 1.0. These special cases are described in more detail in Section 3.3.

3.2. Upper Limits

While in the vast majority of cases, we were able to detect the CLs, the emission features were not detected for a small percentage of the sample, between 4 and 21 sources (i.e., between 3% and 15%) across all five lines (see Table 1). For nondetections, i.e., emission line fluxes with $S/N < 3$, we determined upper limits on the flux. This was done by fixing the centroid wavelength to the expected emission line wavelength (see Appendix C) and the width of the Gaussian to the median of the widths for detected sources, allowing only the amplitude and continuum parameters to vary in our fit. We then fit the spectra with the LMFIT method, and used the resulting flux from this fit as the upper limit flux. To ensure that we provide the most conservative upper limits, we considered the larger flux between that inferred from our original fit (with all parameters free) and that obtained by fixing most parameters, as reported above. The list of sources for which only upper limits were derived is reported in Table 6 in Appendix B.

3.3. Special Cases

In some special cases, we added a second or even a third Gaussian component. Some spectra that had [Ne V] 14.32 μm emission were influenced by the emission of [Cl II] at 14.37 μm, while at longer wavelengths, many sources showed [Fe II] 26.0 μm emission close to the [O IV] 25.89 μm line. A handful of sources showed blueshifted velocity peaks, suggesting the presence of outflowing gas. In some cases, the source showed signatures of both a nearby emission line and a blueshifted velocity peak. Some other spectra showed broad emission lines, where one Gaussian at the center was insufficient for the model to accurately fit the data, and thus, a second Gaussian at the same center wavelength was added. These cases indeed required more attention to detail in the fitting process and will be discussed in the following sections; a detailed breakdown of the number of such cases for each CL can be found in Table 1.

3.3.1. Nearby Emission Lines

For many sources, a close-by, but well-distinguished, emission line is present at redder wavelengths, which would greatly impact our fit, particularly the slope of the continuum, making it difficult to accurately assess the flux of the CLs. For the [Ne V] 14.32 μm and the [O IV] 25.89 μm lines, a second Gaussian was added to the model to account for the emission of [Cl II] 14.37 μm (eight sources or ∼6%) and [Fe II] 26.0 μm (43 sources or ∼31%), respectively. We refer to Table 1 for the number of sources that had a nearby emission line, denoted under "R" for red. For these cases, we took the same steps in calculating the flux and its uncertainty as for the single-Gaussian fits (see Section 3.1), excluding the flux and error of the second Gaussian for the overall reported flux/error. An example of a double-Gaussian fit for the [Ne V] emission at 14.32 μm in the IR spectrum of NGC 4102 is shown in the top right panel of Figure 3.

3.3.2. Blueshifted Lines

A small number of sources, ranging from one to six AGN (i.e., between 0.8% and 4%), display broad emission lines with an asymmetric profile extending to bluer wavelengths, which may be associated with outflowing gas. For these objects, we used two Gaussian lines to account for the blueshifted emission and included the flux from the second Gaussian when calculating the total flux of the line. Table 1 contains the number of sources exhibiting signatures of a blueshifted line, indicated under "O" for outflow. We use "O" to distinguish these objects from those showing a broad emission line, which is denoted as "B" (see Section 3.3.3). An example of a double-Gaussian fit for a [Ne V] 24.32 μm source with a blueshifted line is shown in the bottom left panel of Figure 3. The characteristic width of the Gaussians of these blueshifted/broad lines range from 0.003 to 0.030 μm with a median of 0.010 μm for [Ne V] 14.32 μm, from 0.002 to 0.037 μm with a median of 0.013 μm for [S III] 18.71 μm, from 0.003 to 0.046 μm with a median of 0.017 μm for [Ne V] 24.32 μm, from 0.003 to 0.055 μm with a median of 0.018 μm for [O IV] 25.89 μm, and from 0.003 to 0.071 μm with a median of 0.020 μm for [S III] 33.48 μm (Figure 9). If a line was found to also have a broad and/or a blueshifted component, then the respective characteristic width of the second (and third, if applicable) Gaussian was included in the histogram as an additional data point. See the Sections 3.3.3 and 3.3.4 for a further discussion of these special cases.

3.3.3. Broad Emission Lines

In a few cases, ranging from one to five sources (i.e., between 1% and 4%), the emission lines were broad, and a single Gaussian could not produce a good fit, so a second Gaussian line was added at the same wavelength as the desired emission line. We selected these sources by visually inspecting the single-Gaussian fits, testing the double-Gaussian model fit, and then comparing the values of the χ^2 for the two cases. The total line flux and uncertainty were determined in the same manner as for the sources with blueshifted emission (Section 3.3.2). In Table 1, these are denoted under "B" for broad. It is possible that these broad lines could be interpreted as "symmetric outflows," with simultaneously blueshifted and redshifted outflowing gas (e.g., M. Perna et al. 2017 and A. F. Rojas et al. 2020).

3.3.4. Three Gaussians

Only [Ne V] 14.32 μm and [O IV] 25.89 μm required a model with three Gaussian lines to account for any extra features. A few combinations were needed for such cases: an "outflow" signature, or blueshifted line, with a nearby emission line at longer wavelengths (one source for [Ne V] 14.32 μm and five sources for [O IV] 25.89 μm); a blueshifted line with a broad line (one source for [O IV] 25.89 μm); broad line with a nearby emission at longer wavelengths (two sources for [O IV] 25.89 μm). These are denoted as "O+R," "O+B," and "B+R," respectively, in Table 1. Again, the spectra that required this model were selected by visual inspection and by comparing the χ^2 after the new model fit. The total line flux was calculated according to the specific case. If there was a blueshifted line and/or if the line was broad, then the corresponding flux was added to the total flux. On the other hand, if a Gaussian was added to account for any redder separate emission line, then the flux and uncertainty of the additional line were not considered. An example of a triple-Gaussian fit, specifically for a source showing a blueshifted peak signature along with a nearby emission line, is shown in the bottom right panel of Figure 3.

4. Results and Discussion

Here, we present and discuss the main results of our work. In Section 4.1, we illustrate the detection rates of the MIR CLs studied here, and compare them with the NIR [Si VI] 1.96 μm and [Si X] 1.43 μm CLs measured by J. S. den Brok et al. (2022). In Section 4.2, we discuss the correlation between the CL and the X-ray flux, and how their flux ratios relate to the AGN properties (i.e., $N_{\rm H}$, $M_{\rm BH}$, $L_{14\text{–}150}$, and $\lambda_{\rm Edd}$). The fluxes of all lines studied here are reported in Table 4 of Appendix B.

4.1. Detection Rates

We find that each of the five MIR emission lines studied in this work has very high detection rates (85%–95%), as given in Table 1. The best-fit centroid wavelengths of the lines were consistent with the expected values for each line (see Appendix C). In Figure 4, we compare the detection rate of the MIR CLs with those of [Si VI] and [Si X] lines in the NIR provided by J. S. den Brok et al. (2022) for the Swift/BAT sample. These two emission lines have very high-ionization energies of 167 and 351 eV, respectively, and are found at rest-frame wavelengths of 1.963 and 1.430 μm. Given their high ionizing potentials, they could serve as a useful comparison with the MIR CLs.

The detection rates for all CLs were determined as follows. For each source, we evaluated whether the emission line luminosity error was below a defined threshold luminosity and counted the sources with errors below this value. Sources with a luminosity error exceeding the threshold were excluded from that bin, as their sensitivity was insufficient for detection at the threshold luminosity. Next, for each threshold luminosity bin, we counted how many sources met the detection criterion $(S/N > 3)$. The higher-luminosity bins contain most of the sources, as all observations are sensitive enough to detect a 10^{43} erg s^{-1} line. The detection fraction and its uncertainty were calculated using the SciPy Python package by applying the inverse of the regularized incomplete beta function. This process was repeated for each MIR line, the two NIR lines, and their corresponding X-ray luminosity in the 14–150 keV range. Here and throughout the paper, fractions and uncertainties were estimated following E. Cameron (2011). All the uncertainties represent the 16th and 84th quantiles of a binomial distribution. We performed this test for the NIR lines [Si VI] 1.96 μm and [Si x] 1.43 μm, as well as for our MIR lines. The top and central panels of Figure 4 show that the MIR CLs studied here are typically detected nearly twice as frequently as the silicon lines in the NIR, and thus serve as a better proxy for AGN activity.

In the bottom panel of Figure 4, we show the detection fraction of the five CLs studied here as a function of the ionizing potential. While we do not see a large change in the detection fractions (~10% at most) and do not find evidence of a clear trend, we see that the [Ne v] lines, which have the highest IP, are also those with the lowest detection fraction. In order to understand the origin of the nondetections, we studied whether the AGN for which CLs were not detected have different properties than those in which they are detected. This was done by performing Kolmogorov–Smirnov tests for these two samples to test whether their black hole mass, Eddington ratio, column density, and X-ray luminosities are different. Our test showed that, for none of the CLs studied here, the two subsamples presented significant differences.

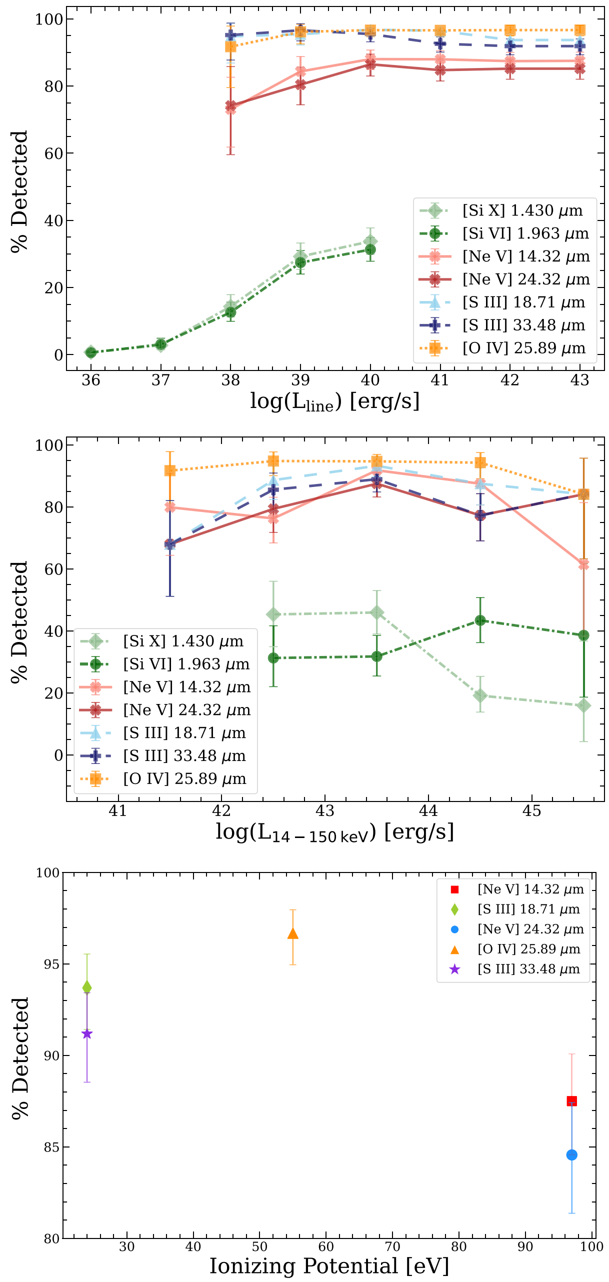

Figure 4. Comparison of the detection fraction for the MIR lines studied in this work with the NIR [Si VI] and [Si X] lines from J. S. den Brok et al. (2022) as a function of the logs of the line (top panel) and hard X-ray (central panel) luminosities. The MIR lines in this work have significant detections in $\gtrsim$85% of local AGN, meaning they are almost twice as likely to be detected than their NIR counterparts. The bottom panel shows the detection rate vs. the ionizing potential for the MIR emission lines studied here.

4.2. The Relation between MIR CLs and AGN Emission

We studied the relations between the coronal emission line flux and the X-ray flux in the 2–10 keV and 14–150 keV bands for each emission line, along with the relation between the

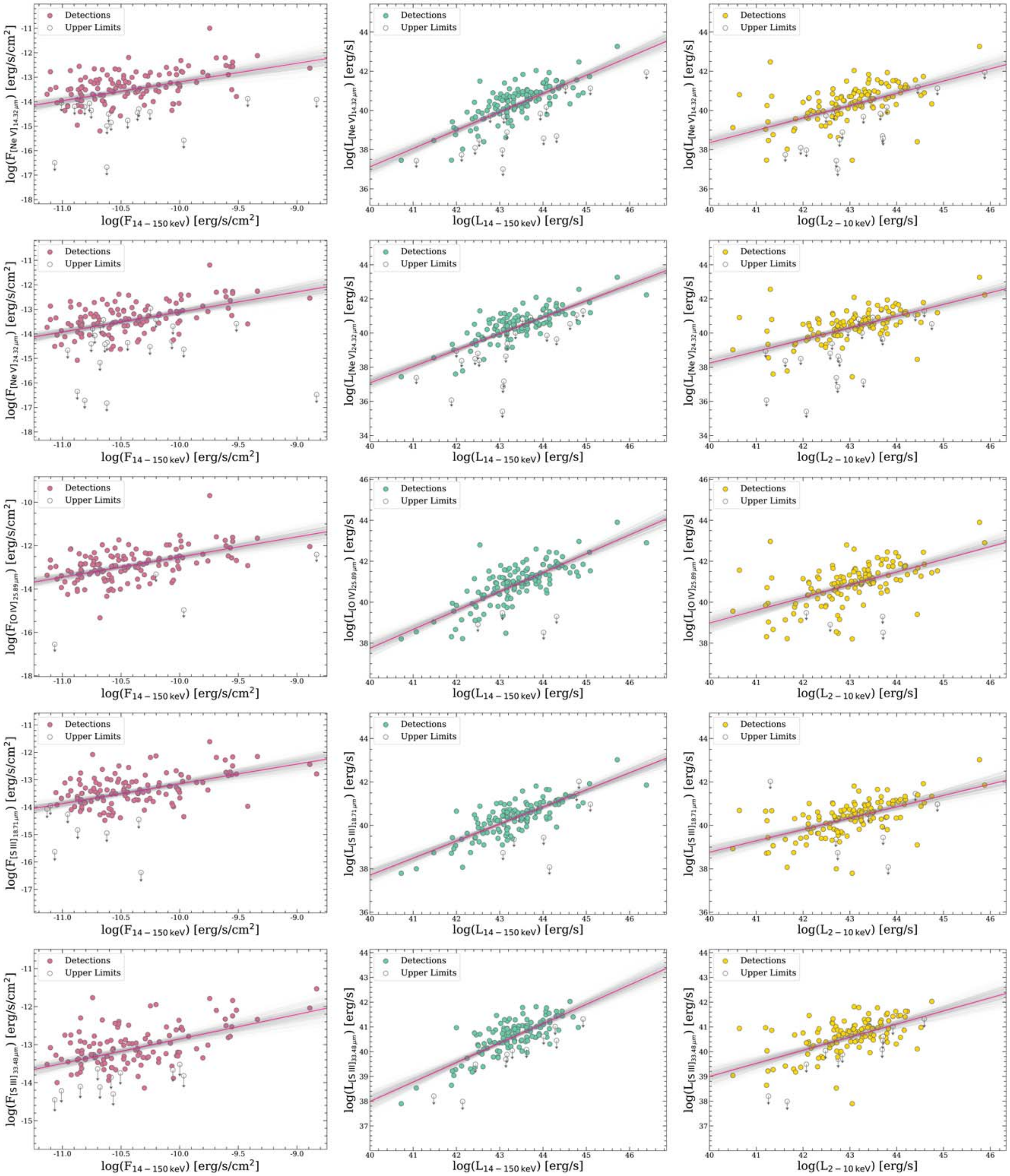

Figure 5. Log of the emission line flux vs. log of the X-ray flux (left panels) and log of emission line luminosity vs. log of X-ray luminosity (central and right panels) for [Ne V] 14.32/24.32 μm, [O IV] 25.89 μm, and [S III] 18.71/33.48 μm. A linear regression fit in the form $\mathrm{Y} = \alpha \cdot \mathrm{X} + \beta$ was performed on the data, where Y and X represent the log of line flux/luminosities and the log of X-ray flux/luminosities, respectively; α and β represent the slope and y-intercept of the linear fits, respectively. The linear fit values can be found in Table 2. The confidence intervals are also shown on the plots.

emission line luminosity versus the X-ray luminosity, shown in Figure 5. The Python package LINMIX was used for censoring, to take upper limits into consideration, for the overall linear regression fit in the form

$$\mathrm{Y} = \alpha \cdot \mathrm{X} + \beta. \tag{1}$$

Here, Y and X represent the log of line flux/luminosities and the log of the X-ray flux/luminosities, respectively, while α and β represent the slope and y-intercept of the linear fits, respectively. The LINMIX package provides a large array of slopes and y-intercept. We use the median slope and y-intercept as the overall line of best-fit parameters. These fit parameters

Table 2
Table of Linear Regression Fit Data Corresponding to the Fits Shown in Figure 5, in the Form: $Y = \alpha^{*}X + \beta$

Emission Line	$L_{14\text{–}150\ \mathrm{keV}}$ versus L_{Line}					$F_{14\text{–}150\ \mathrm{keV}}$ versus F_{Line}				
	Slope (α)	Intercept (β)	σ (dex)	r	p-value	Slope (α)	Intercept (β)	σ (dex)	r	p-value
[Ne V] 14.32 μm	0.93 ± 0.05	−0.3 ± 2.0	0.5	0.7	3.1e-18	0.76 ± 0.10	−5.6 ± 1.0	0.5	0.4	1.5e-04
[Ne V] 24.32 μm	0.96 ± 0.04	−1.4 ± 1.9	0.4	0.8	2.1e-18	0.82 ± 0.08	−4.9 ± 0.9	0.4	0.4	3.3e-02
[O IV] 25.89 μm	0.92 ± 0.05	0.8 ± 2.0	0.5	0.8	4.8e-18	0.93 ± 0.10	−3.2 ± 1.0	0.5	0.5	3.5e-07
[S III] 18.71 μm	0.79 ± 0.04	6.3 ± 1.6	0.3	0.8	5.3e-19	0.72 ± 0.08	−5.9 ± 0.8	0.4	0.5	3.6e-06
[S III] 33.48 μm	0.79 ± 0.04	6.6 ± 1.7	0.2	0.8	2.5e-20	0.65 ± 0.07	−6.4 ± 0.7	0.2	0.6	2.8e-07
Emission Line	$L_{2-10\ \mathrm{keV}}$ versus L_{Line}					F_{2-10} versus F_{Line}				
	Slope (α)	Intercept (β)	σ	r	p-value	Slope (α)	Intercept (β)	σ (dex)	r	p-value
[Ne V] 14.32 μm	0.63 ± 0.06	13.2 ± 2.4	0.8	0.5	1.2e-05	0.76 ± 0.08	−5.3 ± 0.9	0.5	0.5	1.1e-05
[Ne V] 24.32 μm	0.69 ± 0.05	10.8 ± 2.4	0.7	0.5	7.8e-03	0.73 ± 0.07	−5.6 ± 0.8	0.4	0.6	7.1e-07
[O IV] 25.89 μm	0.62 ± 0.05	14.1 ± 2.3	0.7	0.5	3.9e-06	0.80 ± 0.08	−4.3 ± 0.9	0.5	0.5	2.1e-05
[S III] 18.71 μm	0.52 ± 0.05	17.9 ± 1.9	0.5	0.5	3.3e-04	0.61 ± 0.07	−6.9 ± 0.8	0.4	0.5	1.3e-04
[S III] 33.48 μm	0.53 ± 0.04	17.8 ± 1.9	0.4	0.5	3.2e-04	0.48 ± 0.06	−7.9 ± 0.7	0.3	0.5	1.1e-06

Note. Here, Y and X represent the log of line flux/luminosities and the log of X-ray flux/luminosities, respectively, where we included the linear regression data with the log of the 2–10 keV X-ray luminosity. α and β represent the slope and y-intercept of the linear fits, respectively. Using PYMCCORRELATION, we determined the Spearman's rank correlation coefficient, r, and the corresponding p-value.

and their uncertainties are listed in Table 2, along with some correlation coefficients. We also use LINMIX to determine the intrinsic scatter, taking the median value from the LINMIX array, and the PYMCCORRELATION Python package (G. C. Privon et al. 2020) to obtain the Spearman's rank correlation coefficient and the corresponding p-value (P. A. Curran 2014). For the latter two coefficients, the package provided the 16th, 54th, and 84th percentiles, where we only show the 84th percentile values. We also determined confidence intervals and included these in the plots as well, for visual purposes. We find a clear positive correlation between the log of emission line luminosity and the log of X-ray luminosity, although with rather large scatters (typically 0.4–0.5 dex; see Table 2). To test for any redshift-related effect on the correlations, we performed a test considering only sources within 100 Mpc. We found that the intrinsic scatter for this subsample was consistent with that obtained for our full sample. The slopes obtained are generally steeper than those reported for the entire sample.

We also tested how the CLs studied here are correlated with the bolometric luminosity. This was done by using the results of the recent work of K. K. Gupta et al. (2024), who studied the spectral energy distribution of ∼240 unobscured ($N_{\mathrm{H}} < 10^{22}\ \mathrm{cm}^{-2}$) nearby AGN from the Swift/BAT catalog. In their work, they used simultaneous optical/UV photometric data from Swift/UVOT and X-ray spectral data from Swift/XRT, using GALFIT to correct the source magnitudes for host galaxy contamination in the optical/UV and determine the intrinsic AGN fluxes. As illustrated in Figure 6, the log of the CL luminosities is tightly correlated with the bolometric output of the AGN in our sample.

4.3. CLs and Host Galaxy/AGN Properties

To test whether the correlations reported in Section 4.2 and Table 2 can be safely used through a wide range of AGN parameters, we studied how the ratio between the CL and X-ray fluxes changes with the most fundamental AGN properties. This was done for black hole mass, column density, X-ray luminosity, and Eddington ratio. We used survival analysis to take the upper limits into account and to find the median log (flux ratio) values for seven bins of the different properties. We performed this analysis for all five lines, and as shown in the four top panels of Figure 7, there seems to be *no* obvious correlation between the X-ray flux to emission line flux ratios and the AGN properties, with the possible exception of a tentative decrease of [Ne V] 24.32 μm for the highest column densities. Moreover, we found some evidence that unobscured AGN tend to have lower flux ratios, as originally found by T. Liu et al. (2014). We also checked the same ratios but using the bolometric luminosities (K. K. Gupta et al. 2024) instead of the 14–150 keV ones (four bottom panels of Figure 7), and again found no clear trend, with the possible exception of a decrease in the ratio with black hole mass above $\sim 10^{7.5} M_{\odot}$ for [Ne V] 14.32 μm, [Ne V] 24.32 μm, [O IV] 25.89 μm, and [S III] 33.48 μm.

We also tested whether the ratio between lines and X-ray and bolometric flux correlates with the host galaxy inclination. In order to determine the inclination from the observed ratio of the semiminor to semimajor axes of the galaxy, we use 99 measured values from M. J. Koss et al. (2011) and M. J. Koss et al. (2021). For the remaining sources, we follow the prescription outlined in M. J. Koss et al. (2021), adopting a flattening parameter (q_0) value of 0.2 for disk galaxies and 0.34 for early-type galaxies to convert the observed axis ratio into intrinsic inclination. For these 34 sources, we use inclination measurements from Pan-STARRS or the Two Micron All Sky Survey Extended Source Catalog (T. H. Jarrett et al. 2000). In seven cases, typically the most distant and luminous sources, the imaging is completely dominated by the PSF emission, and the host galaxy inclination cannot be reliably measured. We did not find any significant correlation between the inclination angles and the ratio of the CL and X-ray or bolometric fluxes. We also investigated whether the nondetection of the CLs could be associated with a particular range of host galaxy inclinations. A Kolmogorov–Smirnov test showed that, for all CLs studied here, there is no significant difference in the distribution of inclination angles between detections and nondetections.

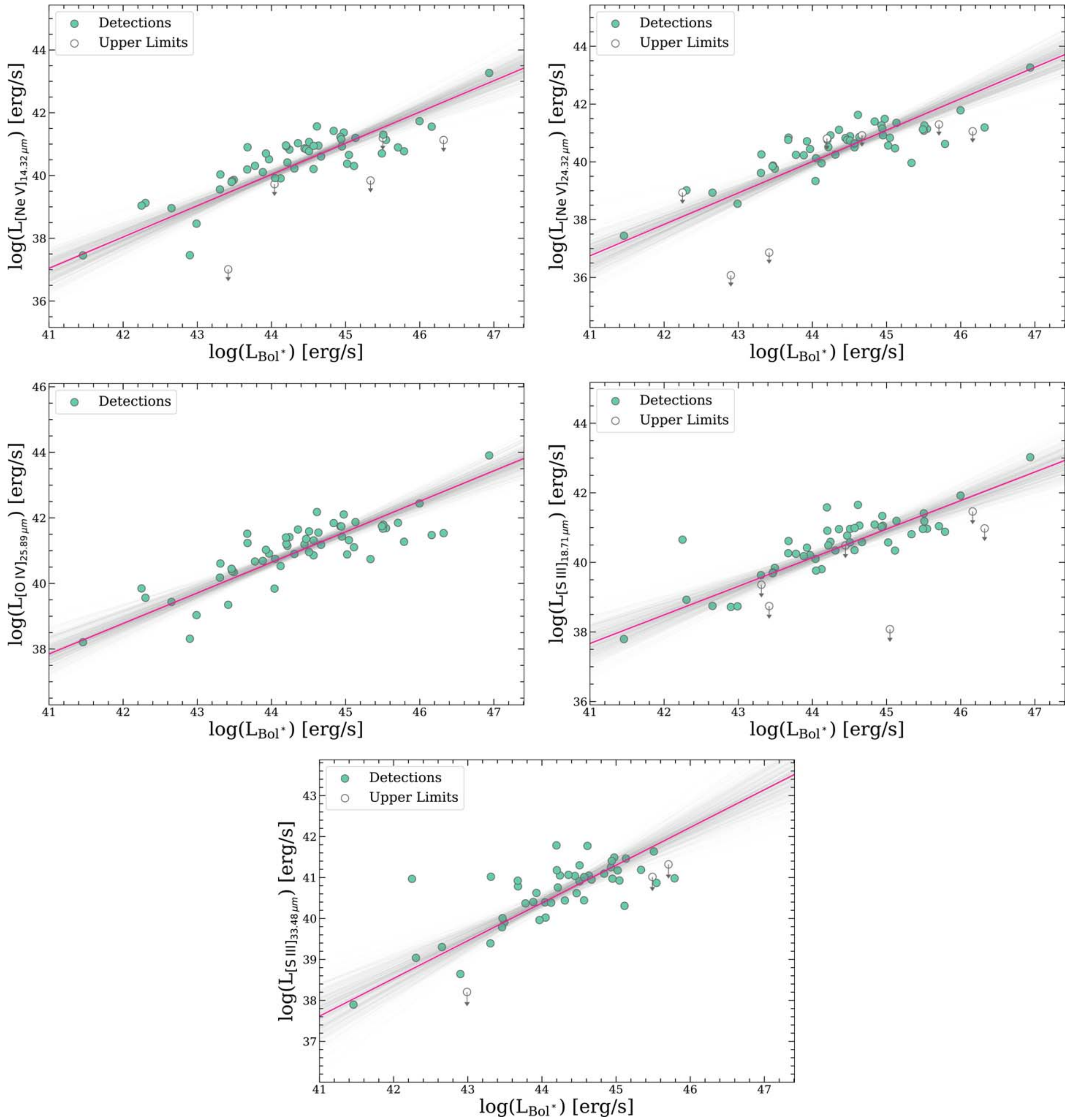

Figure 6. Log of emission line luminosities vs. log of bolometric luminosities (obtained from the spectral energy distribution analysis of K. K. Gupta et al. (2024), represented by L_{bol^*}) for the lines studied here. We performed a linear regression fit in the form $\mathrm{Y} = \alpha \cdot \mathrm{X} + \beta$, where Y and X represent the logs of the line and bolometric luminosities, respectively; α and β represent the slope and y-intercept of the linear fits, respectively. The linear fit values can be found in Table 3, with errors. The confidence intervals on the best fit are shown as shaded areas.

Our results indicate that the MIR forbidden emission lines are generally unbiased to varying AGN properties, further emphasizing how they can be a useful proxy for AGN activity. Studies with larger samples might allow us to better understand the possible relation of the ratio between CL and AGN bolometric luminosities with black hole mass. All correlations reported here could be particularly useful for future observations with JWST in estimating the X-ray and bolometric luminosity of sources once the MIR line fluxes have been determined.

4.4. MIR Coronal and Silicon Lines

We also compared the line fluxes of coronal MIR and silicon lines. We took the sources from J. S. den Brok et al. (2022) that

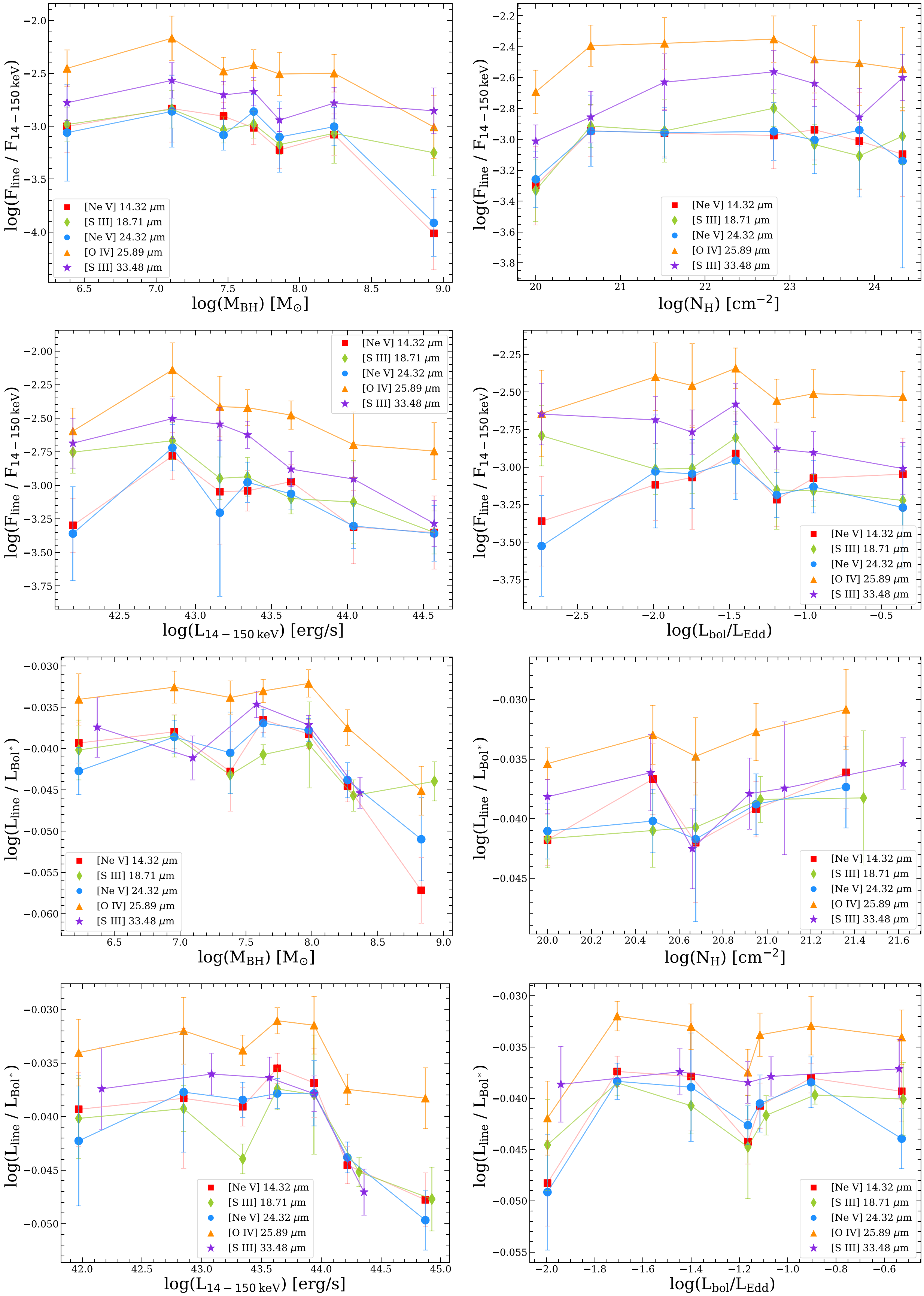

Figure 7. Median ratio between the flux/luminosity of the lines and the 14–150 keV (top four panels) and bolometric (bottom four panels) flux/luminosity for all five emission lines studied here, vs. black hole mass, column density, Eddington ratio, and X-ray luminosity. The filled red squares represent [Ne V] 14.32 μm, the filled green diamonds represent [S III] 18.71 μm, the filled blue circles represent [Ne V] 24.32 μm, the filled orange triangles represent [O IV] 25.89 μm, and the filled purple stars represent [S III] 33.48 μm. The range in N_H is very narrow since the bolometric luminosities in K. K. Gupta et al. (2024) were obtained for a sample of unobscured AGN.

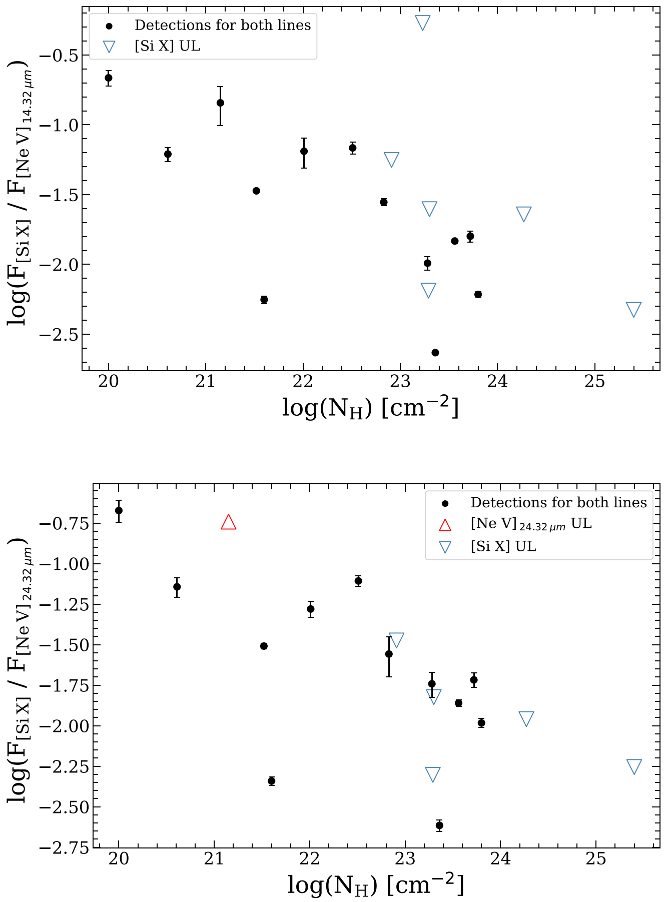

Figure 8. The log of [Si X] 1.43 μm line flux ratio vs. column density with [Ne V] 14.32 μm, top, and [Ne V] 24.32 μm, bottom. The downward triangles represent the upper limits for the silicon sample, while the upward triangles represent an upper limit for [Ne V] 14.32 μm.

overlapped with our sample (22 objects) and calculated the log of the ratio between silicon and MIR CL flux. We then compared this ratio to the different AGN properties. While there is no clear correlation with black hole mass, X-ray luminosity, or Eddington ratio, when this ratio was compared to column density, the line ratios tended to decrease as $N_{\rm H}$ increased. Interestingly, this trend was only present for the [Si X] 1.43 μm lines, and could be associated with extinction at these shorter wavelengths. This declining trend is shown in Figure 8, where we show the log of the [Si X] line flux ratio with [Ne V] at 14.32 μm and 24.32 μm.

4.5. Comparison with Recent Studies

The 140 Swift/BAT-selected objects used in this work are some of the brightest AGN in the sky, and hence have featured in a range of previous studies. K. A. Weaver et al. (2010) had previously studied the MIR spectra of 79 sources selected from an earlier version of the Swift/BAT catalog. In Appendix D, we compare our [Ne V] and [O IV] measurements with K. A. Weaver et al. (2010), and we find good agreement in the 75 sources that overlap with our sample.

Instead of using the ultra-hard X-ray flux, another popular method to identify both obscured and unobscured AGN is via their MIR continuum flux, which probes the thermal emission from warm dust heated by the AGN. The most comprehensive studies using this method have been through the 12 μm-selected sample of 112 AGN (S. Tommasin et al. 2008, 2010). These studies have found that the [Ne V] and [O IV] MIR lines are good tracers of the AGN emission, by comparing them with both their optical emission properties (e.g., A. Feltre et al. 2023) and X-ray properties (L. Spinoglio et al. 2022). A total of 100 of these 12 μm-selected AGN have both Spitzer/IRS and Swift/BAT data, meaning they appear in our sample. These 100 objects were recently studied in detail by L. Spinoglio et al. (2022), who found that the high-ionization MIR [Ne V] and [O IV] lines correlate with other AGN bolometric indicators, and that there is no evidence for systematic differences in these correlations among the various AGN populations, including types 1 and 2 and Compton-thick and Compton-thin AGN, consistent with the conclusions of this work. Furthermore, Equations (1), (2), and (3) of L. Spinoglio et al. (2022) give the observed correlations of

$$L_{\rm bol} \propto L_{[\rm O\,IV]\,25.9}^{0.88\pm0.06} \propto L_{[\rm Ne\,V]\,14.3}^{0.90\pm0.08} \propto L_{[\rm Ne\,V]\,24.3}^{1.06\pm0.10}, \tag{2}$$

which are consistent with the correlations we observe between the MIR emission line luminosities and the 14–150 keV luminosities in Table 2. The bolometric luminosities in L. Spinoglio et al. (2022) were calculated using the bolometric corrections of E. Lusso et al. (2012), while in our work, we used the bolometric luminosities obtained for each source by a careful analysis of their simultaneous optical/UV/X-ray spectral energy distribution. Our study represents a significant increase in sample size compared to previous studies, as this is the largest study to date of Swift/BAT AGN.

5. Summary and Conclusions

In this paper we have studied the relation between MIR forbidden emission lines and the X-ray emission from AGN. By using the MIR spectra from Spitzer/IRS, we carefully modeled the [Ne V] 14.32/24.32 μm, [S III] 18.71/33.48 μm, and [O IV] 25.89 μm CLs (see Figure 3 and Table 1) for a sample of ∼140 Swift/BAT-selected AGN for which black hole mass, column density, X-ray luminosity, and Eddington ratio properties are available. Our main results are:

1. We found a very high detection rate for coronal emission lines in our sample, with at least 85% of the objects showing each of the lines we studied (see Figure 4 and Table 1 for details).
2. The MIR CLs luminosities correlate well with the 14–150 keV luminosities, with a typical scatter of 0.4–0.5 dex, confirming the idea that MIR CLs are good proxies for the accretion power (see Figure 5), at least in the range of X-ray luminosities probed here (10^{42}–10^{45} erg s^{-1}). The relations between the MIR lines studied here and the X-ray emission are reported in Table 2.
3. The CL emission is tightly correlated to the bolometric luminosity ($\sigma \sim 0.2$–0.3 dex), calculated from careful analysis of the spectral energy distribution (K. K. Gupta et al. 2024; Figure 6). The relations between the MIR lines studied here and the bolometric emission are reported in Table 3.
4. The ratio between line flux/luminosity and hard X-ray flux/luminosity is independent of black hole mass, AGN luminosity, and Eddington ratio, and mostly not affected by high X-ray column densities (Figure 7), within the range of parameters studied here. A possible decrease of

Table 3
Table of Linear Regression fit Data Corresponding to the Fits Shown in Figure 6 in the Form $Y = \alpha^* X + \beta$

Emission Line	$L^*_{\rm bol}$ versus $L_{\rm Line}$				
	Slope (α)	Intercept (β)	σ (dex)	r	p-value
[Ne V] 14.32 μm	1.00 ± 0.07	-3.8 ± 3.2	0.3	0.8	1.9e-11
[Ne V] 24.32 μm	1.09 ± 0.08	-7.8 ± 3.7	0.3	0.8	3.6e-10
[O IV] 25.89 μm	0.93 ± 0.06	-0.3 ± 2.7	0.2	0.9	1.1e-12
[S III] 18.71 μm	0.82 ± 0.07	4.0 ± 3.1	0.3	0.8	1.3e-07
[S III] 33.48 μm	0.92 ± 0.09	-0.2 ± 3.8	0.2	0.8	1.6e-07

Note. Here, Y and X represent the logs of the line luminosity and bolometric luminosity (from K. K. Gupta et al. 2024), respectively. α and β represent the slope and y-intercept of the linear fits, respectively. Using PYMCCORRELATION, we determined Spearman's Rank correlation coefficient (r) and the corresponding p-value.

the ratio between the line and bolometric luminosity and the black hole mass is found above $\sim 10^{7.5} M_\odot$ for [Ne V] 14.32 μm, [Ne V] 24.32 μm, [O IV] 25.89 μm, and [S III] 33.48 μm.

Our results show that these lines can reliably serve as proxies for X-ray luminosity, without bias across black hole mass, column density, Eddington ratio, and X-ray luminosity, at least within the ranges of these parameters probed here. Future studies of AGN with JWST will be able to use these CLs to study obscured growth across cosmic time.

Acknowledgments

We thank the referee for the suggestions and very detailed comments, which helped us improve the manuscript. We thank Teng Liu for his useful comments on our work. C.R. acknowledges support from Fondecyt Regular grant 1230345, ANID BASAL project FB210003, and the China-Chile joint research fund. M.J.T. acknowledges support from a FONDECYT postdoctoral fellowship (3220516). Y.D. acknowledges support from a FONDECYT postdoctoral fellowship (3230310). J.M.C.'s contribution was supported by an appointment to the NASA Postdoctoral Program at the NASA Goddard Space Flight Center, administered by Oak Ridge Associated Universities under contract with NASA. R.R. acknowledges support from the Fundación Jesús Serra and the Instituto de Astrofísica de Canarias under the Visiting Researcher Programme 2023–2025 agreed between both institutions. R.R. also acknowledges support from the ACIISI, Consejería de Economía, Conocimiento y Empleo del Gobierno de Canarias and the European Regional Development Fund (ERDF) under grant with reference ProID2021010079, and the support through the RAVET project by the grant PID2019-107427GB-C32 from the Spanish Ministry of Science, Innovation and Universities MCIU. This work has also been supported through the IAC project TRACES, which is partially supported by the state budget and the regional budget of the Consejería de Economía, Industria, Comercio y Conocimiento of the Canary Islands Autonomous Community. RR also thanks to Conselho Nacional de Desenvolvimento Científico e Tecnológico (CNPq, Proj. 311223/2020-6, 304927/2017-1 and 400352/2016-8), Fundação de amparo à pesquisa do Rio Grande do Sul (FAPERGS, Proj. 16/2551-0000251-7 and 19/1750-2), Coordenação de Aperfeiçoamento de Pessoal de Nível Superior (CAPES, Proj. 0001). This work was funded by ANID through CATA-BASAL FB210003 (FEB); FONDECYT Regular 1200495 (FEB) and 1241005 (FEB); and Millennium Science Initiative AIM23-0001 and ICN12_009 (FEB). K.K.G. thanks the Belgian Federal Science Policy Office (BEL- SPO) for the provision of financial support in the framework of the PRODEX Programme of the European Space Agency (ESA). A.R.L. acknowledges support from a FONDECYT postdoctoral fellowship (3210157). The work of DS was carried out at the Jet Propulsion Laboratory, California Institute of Technology, under a contract with NASA.

Facility: Swift, Wide-field Infrared Survey Explorer, IRAS, Spitzer, Akari.

Appendix A
Excluded Sources

There are some cases that required us to exclude the spectra for source(s) from analyses. The source SDSS J130005.35+163214.8 only had an HR spectrum with the range of 9–18 μm, and thus could not be analyzed for [S III] 18.7078 μm, [Ne V] 24.32 μm, [O IV] 25.89 μm, and [S III] 33.48 μm. When evaluating [S III] 18.7078 μm, three other sources (NGC 985, IRAS 05189−2524, and UGC 5101) had missing pixels in their Spitzer spectra that greatly affected the fit. Therefore, these were also excluded from analyses. When evaluating [S III] 33.48 μm, we noticed quite a few problems with some spectra. For Mrk 352, most of the flux density pixels were "zero," thus a model fit was incalculable. Additionally, the spectra for PG 0026+129, 3C 234, 3C 273, Q 1821+643, and PG 2349−014 had redshifted out enough to not include the rest-frame 25.89 μm CL. Lastly, for the sources PG 0804+761 and 4C +74.26, their spectra were partially redshifted out, but did not have enough flux density for a proper fit, and therefore were excluded from analyses.

Appendix B
CL Fluxes

In Table 4 and 5, we report the fluxes of all MIR lines studied here, while the list of sources for which only upper limits are available is shown in Table 6.

Table 4

Table of Spitzer/IRS Fluxes and Model Information for [Ne V] 14.32 μm, [Ne V] 24.32 μm, and [O IV] 25.89 μm s^{-1}

SWIFT ID (1)	Source Name (2)	z (3)	[Ne V] 14.32 μm d.o.f (4)	Model (5)	[Ne V] 24.32 μm d.o.f (6)	Model χ^2 (7)	[O IV] 25.89 μm d.o.f (8)	Model χ^2 (9)
SWIFT J0006.2+2012	Mrk 335	0.0258	1.1 ± 0.2	S	2.2 ± 0.3	S	4.9 ± 0.3	S
			17	0.8	18	1.1	21	1.6
SWIFT J0029.2+1319	PG 0026+129	0.142	0.7 ± 0.1	S	⩽0.2	S	0.6 ± 0.0	S
			17	1.7	18	3.3	19	12.5
SWIFT J0042.9−2332	NGC 235A	0.0222	3.5 ± 0.2	S	5.1 ± 0.2	S	15.2 ± 0.5	D, R
			16	0.4	19	0.8	16	0.7
SWIFT J0048.8+3155	Mrk 348	0.015	6.2 ± 0.2	S	4.5 ± 0.8	S	15.8 ± 0.9	S
			16	2.1	19	0.4	19	4.1
SWIFT J0059.4+3150	Mrk 352	0.0149	⩽0.0	S	⩽0.0	S	0.5 ± 0.1	D, R
			17	1.7	20	3.5	16	5.3
SWIFT J0111.4−3808	NGC 424	0.0118	12.4 ± 0.6	S	6.6 ± 0.8	S	26.0 ± 1.5	D, B
			16	1.1	18	0.6	16	0.8
SWIFT J0114.4−5522	NGC 454	0.0121	3.1 ± 0.2	S	5.1 ± 0.4	S	14.7 ± 0.5	D, R
			16	1.4	19	0.7	17	2.7
SWIFT J0123.8−3504	NGC 526A	0.0191	2.7 ± 0.6	S	3.4 ± 0.3	S	15.7 ± 0.2	S
			16	1.2	19	4.7	19	5.4
SWIFT J0123.9−5846	Fairall 9	0.047	2.7 ± 0.3	S	2.7 ± 0.4	S	9.6 ± 0.3	T, B+R
			17	1.8	15	3.5	14	5.4
SWIFT J0124.5+3350	NGC 513	0.0195	⩽0.8	S	0.9 ± 0.1	S	4.7 ± 0.1	D, R
			19	0.4	18	1.6	17	3.3
SWIFT J0127.5+1910	Mrk 359	0.0174	3.1 ± 0.3	S	2.6 ± 0.3	S	7.0 ± 0.3	S
			16	1.0	19	0.3	19	0.8
SWIFT J0138.6−4001	ESO 297−18	0.0252	0.4 ± 0.1	S	⩽0.5	S	2.0 ± 0.4	S
			17	0.7	20	2.1	20	1.4
SWIFT J0152.8−0329	MCG −1−5−47	0.0172	0.1 ± 0.0	S	⩽0.1	S	0.0 ± 0.0	S
			15	4.4	18	3.0	19	4.8
SWIFT J0201.0−0648	NGC 788	0.0136	5.5 ± 0.1	S	6.9 ± 1.0	S	19.1 ± 1.1	S
			16	0.9	19	1.2	19	2.0
SWIFT J0214.6−0049	Mrk 590	0.0264	0.7 ± 0.1	S	1.2 ± 0.3	S	2.6 ± 0.2	S
			16	1.7	18	2.0	21	1.9
SWIFT J0228.1+3118	Mrk 1040	0.0167	11.0 ± 0.7	S	13.6 ± 0.8	S	42.4 ± 0.6	S
			16	0.5	19	0.7	19	2.2
SWIFT J0230.2−0900	Mrk 1044	0.0165	⩽0.9	S	0.4 ± 0.0	S	1.2 ± 0.1	D, R
			18	1.3	17	6.0	16	1.4
SWIFT J0231.6−3645	IC 1816	0.017	8.1 ± 0.2	S	3.8 ± 0.1	S	14.1 ± 0.2	D, R
			17	2.0	18	0.6	17	5.3
SWIFT J0234.1+3233	NGC 973	0.0162	2.5 ± 0.2	S	2.9 ± 0.1	S	11.8 ± 0.3	D, R
			17	1.1	18	0.9	17	1.8
SWIFT J0234.6−0848	NGC 985	0.043	5.5 ± 0.3	S	7.3 ± 0.3	S	30.1 ± 0.3	S
			17	2.0	16	3.2	20	10.4
SWIFT J0238.2−5213	ESO 198−24	0.0455	⩽0.3	S	0.9 ± 0.1	S	0.8 ± 0.1	S
			19	1.1	16	1.3	21	3.9
SWIFT J0241.3−0816	NGC 1052	0.005	⩽0.1	S	⩽0.4	S	2.6 ± 0.4	D, R
			18	0.9	21	1.1	16	2.1
SWIFT J0242.6+0000	NGC 1068	0.0038	1003.4 ± 9.7	D, B	641.0 ± 11.7	S	20197.9 ± 3235.0	T, B+R
			13	3.2	18	6.4	13	2.9
SWIFT J0251.6−1639	NGC 1125	0.011	4.8 ± 0.2	S	10.0 ± 0.7	S	34.4 ± 0.3	D, R
			16	0.9	18	0.2	16	2.1
SWIFT J0255.2−0011	NGC 1142	0.0289	⩽0.0	S	⩽0.2	S	⩽0.1	S
			16	3.5	19	1.0	20	1.2
SWIFT J0256.4−3212	ESO 417−6	0.0163	0.4 ± 0.0	D, R	0.7 ± 0.0	S	3.3 ± 0.1	D, R
			14	0.9	17	1.8	17	1.0
SWIFT J0304.1−0108	NGC 1194	0.0136	4.1 ± 0.3	S	3.4 ± 0.4	S	299.1 ± 14.4	S
			16	0.5	19	2.6	19	1.0
SWIFT J0433.0+0521	3C 120	0.033	13.9 ± 0.4	S	21.8 ± 0.6	S	108.2 ± 1.3	S
			17	1.3	17	2.7	21	4.2
SWIFT J0436.3−1022	Mrk 618	0.0355	4.1 ± 0.3	D, O	2.7 ± 0.3	S	13.6 ± 1.3	D, O
			14	0.9	17	1.2	18	4.3
SWIFT J0451.4−0346	MCG −1−13−25	0.0159	⩽0.1	S	0.2 ± 0.0	S	1.0 ± 0.0	D, R
			18	1.2	17	9.8	17	2.4
SWIFT J0456.3−7532	ESO 33−2	0.0181	5.7 ± 0.5	S	5.0 ± 0.2	S	13.2 ± 0.1	S
			17	2.4	19	0.8	19	7.8

Table 4
(Continued)

SWIFT ID (1)	Source Name (2)	z (3)	[Ne V] 14.32 μm d.o.f (4)	Model (5)	[Ne V] 24.32 μm d.o.f (6)	Model χ^2 (7)	[O IV] 25.89 μm d.o.f (8)	Model χ^2 (9)
SWIFT J0508.1+1727	2MASX J05081967 +1721483	0.0175	1.9 ± 0.3	S	⩽2.2	S	8.1 ± 0.5	S
			16	0.8	21	0.3	19	0.7
SWIFT J0516.2−0009	Ark 120	0.0323	1.0 ± 0.2	S	1.6 ± 0.4	S	3.3 ± 0.2	D, R
			17	1.0	18	0.5	18	1.8
SWIFT J0501.9−3239	ESO 362−18	0.0125	2.4 ± 0.1	S	2.6 ± 0.1	S	10.0 ± 0.2	S
			16	1.5	18	0.6	19	2.8
SWIFT J0521.0−2522	IRAS 05189−2524	0.0426	16.7 ± 0.2	D, O	13.6 ± 0.1	S	21.6 ± 1.2	S
			20	2.9	17	2.9	22	2.6
SWIFT J0552.2−0727	NGC 2110	0.0078	3.1 ± 0.3	S	5.6 ± 0.3	S	27.2 ± 0.5	D, R
			16	4.1	18	3.7	15	6.8
SWIFT J0557.9−3822	H0 557−385	0.0339	3.1 ± 0.3	S	1.7 ± 0.2	S	4.6 ± 0.2	S
			17	0.9	17	1.2	21	5.3
SWIFT J0601.9−8636	ESO 5−4	0.0062	⩽0.4	S	⩽0.3	S	1.7 ± 0.1	D, R
			18	1.7	20	0.5	14	0.6
SWIFT J0615.8+7101	Mrk 3	0.0135	62.3 ± 0.9	S	55.5 ± 1.0	S	174.2 ± 2.1	S
			16	4.6	19	3.5	20	11.6
SWIFT J0651.9+7426	Mrk 6	0.0188	11.5 ± 0.4	S	9.3 ± 0.5	S	45.9 ± 0.1	D, B
			17	1.6	19	1.8	16	2.5
SWIFT J0655.8+3957	UGC 3601	0.0171	1.9 ± 0.1	S	2.5 ± 0.1	S	12.6 ± 0.1	D, R
			17	2.3	17	2.1	17	7.3
SWIFT J0725.8+3000	Z 147−20	0.0188	⩽0.6	S	⩽0.0	S	0.9 ± 0.2	D, R
			19	1.9	21	0.3	16	0.6
SWIFT J0736.9+5846	Mrk 9	0.0399	2.0 ± 0.2	S	1.8 ± 0.3	S	4.3 ± 0.1	S
			17	1.6	16	2.0	21	2.1
SWIFT J0742.5+4948	Mrk 79	0.0222	9.8 ± 0.5	S	11.8 ± 0.3	S	40.6 ± 1.2	S
			16	1.7	18	0.8	19	16.3
SWIFT J0800.1+2638	IC 486	0.0269	2.8 ± 0.1	S	2.5 ± 0.1	S	11.0 ± 0.1	S
			17	1.0	18	1.6	21	5.9
SWIFT J0807.9+3859	Mrk 622	0.0232	1.3 ± 0.1	S	⩽0.9	S	7.2 ± 0.1	S
			16	1.7	21	3.6	20	6.0
SWIFT J0810.9+7602	PG 0804+761	0.1	⩽0.6	S	0.5 ± 0.1	S	1.9 ± 0.1	S
			18	1.1	19	1.5	21	2.8
SWIFT J0856.0+7812	NGC 2655	0.0047	1.2 ± 0.1	S	0.1 ± 0.0	S	1.0 ± 0.2	D, R
			16	5.4	17	4.9	16	4.8
SWIFT J0902.0+6007	Mrk 18	0.0111	0.4 ± 0.1	S	0.8 ± 0.2	S	2.1 ± 0.1	D, R
			16	3.5	18	2.5	16	5.6
SWIFT J0918.5+1618	Mrk 704	0.0292	3.6 ± 0.2	S	3.0 ± 0.1	S	12.0 ± 0.5	S
			17	1.3	18	0.6	21	2.8
SWIFT J0920.8−0805	MCG −1−24−12	0.0196	2.2 ± 0.2	S	2.2 ± 0.3	S	9.7 ± 0.2	S
			17	0.5	19	3.9	19	3.5
SWIFT J0923.7+2255	Z 121−75	0.0323	1.6 ± 0.2	S	1.2 ± 0.1	S	7.3 ± 0.1	S
			17	1.4	17	1.7	21	2.4
SWIFT J0925.0+5218	Mrk 110	0.0353	0.7 ± 0.1	S	1.0 ± 0.2	S	4.5 ± 0.2	S
			17	1.5	16	3.3	21	3.8
SWIFT J0926.2+1244	Mrk 705	0.0291	3.1 ± 0.1	S	2.9 ± 0.1	S	4.8 ± 0.4	S
			17	1.8	18	0.8	21	2.1
SWIFT J0935.9+6120	UGC 5101	0.0394	4.2 ± 0.4	D, R	3.3 ± 0.4	D, O	6.3 ± 0.5	T, O+R
			14	1.0	14	1.6	15	2.2
SWIFT J0945.6−1420	NGC 2992	0.0077	20.3 ± 0.3	S	25.4 ± 0.7	S	109.3 ± 1.1	D, R
			16	6.4	18	1.7	16	6.5
SWIFT J0947.6−3057	MCG −5−23−16	0.0085	11.7 ± 0.6	S	8.1 ± 0.5	S	19.7 ± 0.5	S
			16	1.3	18	0.6	18	1.0
SWIFT J0959.5−2248	NGC 3081	0.008	29.5 ± 0.5	S	38.0 ± 0.5	S	117.6 ± 0.6	S
			16	4.5	18	1.8	19	2.3
SWIFT J1001.8+2848	3C 234	0.1849	3.2 ± 0.2	S	3.8 ± 0.8	D, O	9.8 ± 0.5	S
			16	1.3	16	2.1	21	0.6
SWIFT J1001.7+5543	NGC 3079	0.0037	0.9 ± 0.1	S	1.0 ± 0.3	S	8.6 ± 1.0	D, R
			16	10.5	18	1.1	16	2.0
SWIFT J1023.5+1952	NGC 3227	0.0039	22.2 ± 0.5	S	17.8 ± 0.6	D, B	67.6 ± 0.6	D, R
			16	1.0	15	2.4	16	6.6
SWIFT J1031.7−3451	NGC 3281	0.0107	48.0 ± 1.2	S	39.6 ± 1.5	S	162.7 ± 1.8	S

Table 4
(Continued)

SWIFT ID (1)	Source Name (2)	z (3)	[Ne V] 14.32 μm d.o.f (4)	Model (5)	[Ne V] 24.32 μm d.o.f (6)	Model χ^2 (7)	[O IV] 25.89 μm d.o.f (8)	Model χ^2 (9)
			17	1.4	17	1.8	18	4.8
SWIFT J1048.4−2511	NGC 3393	0.0125	20.5 ± 0.4	S	41.2 ± 0.7	S	183.3 ± 1.8	D, B
			16	4.9	18	2.6	17	3.3
SWIFT J1106.5+7234	NGC 3516	0.0088	4.9 ± 0.3	S	8.0 ± 0.2	S	33.5 ± 0.5	S
			16	1.0	18	1.5	18	9.6
SWIFT J1139.0−3743	NGC 3783	0.0097	16.1 ± 0.6	S	13.7 ± 0.8	S	40.1 ± 0.5	S
			16	1.3	19	1.2	19	4.8
SWIFT J1139.8+3157	NGC 3786	0.0089	2.3 ± 0.1	S	2.6 ± 0.2	S	12.9 ± 2.0	D, B
			16	2.6	19	1.2	15	1.7
SWIFT J1143.7+7942	UGC 6728	0.0065	1.0 ± 0.1	S	0.9 ± 0.2	S	3.0 ± 0.0	S
			16	1.2	18	4.2	19	3.0
SWIFT J1157.8+5529	NGC 3998	0.0035	0.1 ± 0.0	S	⩽0.0	S	0.8 ± 0.1	T, O+R
			16	1.7	19	2.4	13	1.2
SWIFT J1203.0+4433	NGC 4051	0.0023	11.7 ± 0.3	S	9.2 ± 0.3	S	32.3 ± 1.1	D, R
			16	2.7	18	0.4	15	1.1
SWIFT J1204.9+3105	UGC 7064	0.025	3.8 ± 0.2	S	4.5 ± 0.1	S	11.0 ± 0.2	D, R
			17	1.1	16	5.8	17	3.3
SWIFT J1206.2+5243	NGC 4102	0.0028	2.9 ± 0.3	D, R	⩽3.8	S	⩽4.8	S
			13	0.7	20	0.8	20	5.2
SWIFT J1209.4+4340	NGC 4138	0.003	0.5 ± 0.2	S	0.3 ± 0.1	S	0.9 ± 0.2	S
			16	2.0	16	4.1	19	2.9
SWIFT J1210.5+3924	NGC 4151	0.0033	76.0 ± 1.2	S	55.2 ± 1.4	S	220.6 ± 3.3	S
			16	3.3	18	3.4	20	91.8
SWIFT J1218.5+2952	NGC 4253	0.0129	21.9 ± 0.3	S	19.0 ± 0.3	S	47.3 ± 1.0	S
			16	3.4	19	0.9	19	8.7
SWIFT J1219.4+4720	NGC 4258	0.0017	⩽0.4	S	⩽0.4	S	5.8 ± 0.2	D, R
			18	1.6	20	2.1	17	2.5
SWIFT J1225.8+1240	NGC 4388	0.0084	41.5 ± 0.6	S	52.8 ± 1.5	S	240.2 ± 3.2	S
			17	3.4	18	1.2	18	16.3
SWIFT J1202.5+3332	NGC 4395	0.0011	1.1 ± 0.1	S	1.1 ± 0.3	S	6.2 ± 0.2	D, R
			16	1.2	16	1.4	16	2.5
SWIFT J1229.1+0202	3C 273	0.1583	⩽1.3	S	2.6 ± 0.4	S	12.0 ± 0.1	T, O+B
			17	1.0	19	4.3	12	6.4
SWIFT J1232.1+2009	Mrk 771	0.063	0.9 ± 0.1	S	0.9 ± 0.2	S	2.9 ± 0.1	S
			16	1.1	17	0.6	18	2.0
SWIFT J1235.6−3954	NGC 4507	0.0118	12.7 ± 2.7	D, O	11.1 ± 0.5	D, O	33.3 ± 5.9	T, O+R
			13	3.0	15	0.8	13	3.2
SWIFT J1238.6+0928	SDSS J123843.43 +092736.6	0.0829	2.0 ± 0.1	S	2.2 ± 0.3	S	5.8 ± 0.4	S
			16	2.0	18	1.5	20	1.9
SWIFT J1239.6−0519	NGC 4593	0.009	3.8 ± 0.2	S	4.3 ± 0.4	S	13.7 ± 0.2	D, R
			16	2.5	19	2.6	15	2.5
SWIFT J1246.6+5435	NGC 4686	0.0167	0.3 ± 0.0	S	0.2 ± 0.1	S	1.0 ± 0.0	D, R
			16	1.3	18	1.1	16	4.4
SWIFT J1252.3−1323	NGC 4748	0.0146	3.3 ± 0.4	S	12.4 ± 0.5	S	70.7 ± 1.3	S
			17	0.7	19	9.0	20	22.8
SWIFT J1300.1+1635	SDSS J130005.35 +163214.8	0.08	0.6 ± 0.2	S	N/A	N/A	N/A	N/A
			16	0.8	N/A	N/A	N/A	N/A
SWIFT J1304.3−0532	NGC 4941	0.004	7.6 ± 0.1	S	6.3 ± 0.3	S	25.7 ± 0.7	D, R
			16	3.7	18	1.3	15	3.3
SWIFT J1304.3−1022	NGC 4939	0.0104	12.3 ± 0.1	S	16.0 ± 0.2	S	60.0 ± 0.5	S
			16	3.9	19	4.5	18	8.8
SWIFT J1305.4−4928	NGC 4945	0.0019	⩽1.2	S	⩽0.0	S	⩽39.3	S
			18	0.9	20	4.3	21	3.6
SWIFT J1306.4 −4025A	ESO 323−77	0.015	6.2 ± 0.9	S	6.0 ± 0.7	S	21.3 ± 0.4	D, R
			16	0.7	19	2.2	16	5.0
SWIFT J1322.2−1641	MCG −3−34−64	0.0165	64.0 ± 0.5	D, B	37.5 ± 1.8	D, O	110.9 ± 1.3	T, O+R
			13	2.1	16	0.7	13	1.0
SWIFT J1325.4−4301	Cen A	0.0018	23.4 ± 0.6	S	28.7 ± 5.1	S	90.4 ± 4.2	S
			16	4.7	17	4.1	20	16.1

Table 4
(Continued)

SWIFT ID (1)	Source Name (2)	z (3)	[Ne V] 14.32 μm d.o.f (4)	Model (5)	[Ne V] 24.32 μm d.o.f (6)	Model χ^2 (7)	[O IV] 25.89 μm d.o.f (8)	Model χ^2 (9)
SWIFT J1335.8−3416	MCG −6−30−15	0.0077	4.9 ± 0.2	S	5.5 ± 0.5	S	21.9 ± 0.8	S
			16	1.9	18	2.2	17	2.8
SWIFT J1341.9+3537	NGC 5273	0.0035	1.1 ± 0.1	D, R	1.4 ± 0.2	S	4.1 ± 0.0	S
			13	4.5	18	5.3	18	3.1
SWIFT J1349.3−3018	IC 4329A	0.016	30.1 ± 0.9	S	32.7 ± 1.1	S	99.0 ± 1.1	S
			16	1.0	19	1.1	19	8.4
SWIFT J1352.8+6917	Mrk 279	0.0304	4.2 ± 0.1	D, O	2.1 ± 0.1	S	10.0 ± 0.1	S
			14	1.1	17	4.6	21	21.1
SWIFT J1355.9+1822	Mrk 463	0.0504	18.5 ± 0.5	S	20.9 ± 0.6	D, O	67.6 ± 0.2	D, O
			17	4.5	13	11.0	18	10.2
SWIFT J1413.2−0312	NGC 5506	0.0062	61.7 ± 3.3	D, B	50.1 ± 1.4	S	254.3 ± 3.0	D, B
			13	3.1	18	1.3	14	16.3
SWIFT J1417.9+2507	NGC 5548	0.0172	2.6 ± 0.3	S	2.7 ± 0.3	S	12.2 ± 0.2	S
			17	1.8	18	1.4	19	3.8
SWIFT J1429.2+0118	Mrk 1383	0.0865	1.1 ± 0.2	S	1.0 ± 0.1	S	3.4 ± 0.3	S
			16	1.2	18	1.7	19	3.0
SWIFT J1432.8−4412	NGC 5643	0.004	27.1 ± 0.4	S	23.0 ± 0.6	S	79.5 ± 1.9	S
			16	2.5	18	4.1	20	5.2
SWIFT J1433.9+0528	NGC 5674	0.0249	1.8 ± 0.1	S	2.2 ± 0.1	S	6.6 ± 0.1	D, R
			17	1.0	17	5.3	17	2.5
SWIFT J1436.4+5846	Mrk 817	0.0314	1.8 ± 0.3	S	⩽3.7	S	6.8 ± 0.3	S
			17	0.8	20	1.6	21	4.0
SWIFT J1442.5−1715	NGC 5728	0.0093	17.3 ± 0.4	S	24.9 ± 0.3	S	86.2 ± 0.8	S
			16	4.6	18	5.4	17	21.7
SWIFT J1457.8−4308	IC 4518A	0.0163	21.8 ± 0.4	S	21.0 ± 1.7	S	77.2 ± 0.3	D, R
			17	1.9	18	0.6	17	11.2
SWIFT J1504.2+1025	Mrk 841	0.0364	8.8 ± 0.3	S	8.3 ± 0.9	D, B	23.2 ± 0.3	S
			17	2.4	14	1.8	21	2.4
SWIFT J1512.0−2119	IRAS 15091−2107	0.0446	8.1 ± 0.2	S	9.3 ± 1.3	S	33.2 ± 0.5	S
			17	5.3	16	1.5	21	27.7
SWIFT J1515.0+4205	NGC 5899	0.0086	5.5 ± 0.3	S	5.0 ± 0.2	S	19.0 ± 0.3	S
			16	5.3	17	2.7	19	7.8
SWIFT J1548.5−1344	NGC 5995	0.0252	6.0 ± 0.4	S	4.1 ± 0.5	S	11.5 ± 0.4	D, R
			17	0.6	18	0.8	17	4.2
SWIFT J1628.1+5145	Mrk 1498	0.0547	4.0 ± 0.2	S	6.5 ± 0.2	S	24.0 ± 0.7	S
			17	2.9	17	1.1	19	2.8
SWIFT J1652.0 −5915B	NGC 6221	0.005	2.0 ± 0.6	D, R	⩽1.6	S	13.0 ± 2.8	D, R
			13	1.0	21	0.5	16	0.5
SWIFT J1652.9+0223	NGC 6240	0.0245	1.6 ± 0.5	D, R	⩽2.6	S	20.6 ± 2.8	D, R
			14	0.4	20	1.3	17	1.5
SWIFT J1717.1−6249	NGC 6300	0.0037	12.7 ± 0.4	S	8.3 ± 0.6	S	28.9 ± 0.7	S
			16	1.4	18	0.7	18	2.9
SWIFT J1822.0+6421	Q 1821+643	0.297	6.7 ± 0.8	D, B	6.6 ± 0.3	S	28.9 ± 0.4	S
			14	1.2	17	7.5	21	7.9
SWIFT J1836.9−5924	Fairall 49	0.0202	27.8 ± 0.8	S	15.6 ± 3.3	D, B	42.2 ± 0.4	D, R
			17	4.7	15	0.9	17	8.4
SWIFT J1838.4−6524	ESO 103−35	0.0133	16.1 ± 1.6	D, B	9.1 ± 1.5	S	27.7 ± 0.9	D, R
			13	1.4	18	0.3	16	3.7
SWIFT J1842.0+7945	3C 390.3	0.0561	0.8 ± 0.3	S	0.6 ± 0.2	S	2.6 ± 0.6	S
			17	2.5	18	0.8	20	2.4
SWIFT J1844.5−6221	Fairall 51	0.0142	6.5 ± 0.4	S	4.2 ± 0.8	S	24.4 ± 0.7	S
			16	0.4	18	1.2	18	9.3
SWIFT J1848.0−7832	LEDA 89032	0.0741	0.4 ± 0.1	S	1.0 ± 0.1	S	4.3 ± 0.1	D, R
			16	0.8	18	6.8	16	2.2
SWIFT J1921.1−5842	ESO 141−55	0.036	1.5 ± 0.2	S	2.3 ± 0.4	S	7.2 ± 0.2	S
			17	0.8	17	4.2	22	2.7
SWIFT J1942.6−1024	NGC 6814	0.0058	5.0 ± 0.3	S	5.7 ± 0.2	S	20.8 ± 0.4	S
			16	3.0	19	3.0	18	4.8
SWIFT J2009.0−6103	NGC 6860	0.0149	2.6 ± 0.2	S	3.5 ± 0.6	S	10.0 ± 0.8	S
			16	0.4	18	0.8	19	5.1
SWIFT J2042.3+7507	4C +74.26	0.104	⩽0.5	S	0.6 ± 0.1	S	1.3 ± 0.1	S

Table 4
(Continued)

SWIFT ID (1)	Source Name (2)	z (3)	[Ne V] 14.32 μm d.o.f (4)	Model (5)	[Ne V] 24.32 μm d.o.f (6)	Model χ^2 (7)	[O IV] 25.89 μm d.o.f (8)	Model χ^2 (9)
			19	1.5	19	10.1	21	1.2
SWIFT J2044.2−1045	Mrk 509	0.0344	5.9 ± 0.3	S	8.4 ± 0.2	S	27.9 ± 0.3	S
			17	2.6	17	1.5	22	7.4
SWIFT J2052.0−5704	IC 5063	0.0114	25.1 ± 0.6	S	26.8 ± 1.0	S	107.4 ± 1.5	S
			16	2.9	19	0.5	18	2.2
SWIFT J2148.3−3454	NGC 7130	0.0162	7.7 ± 0.6	D, R	4.7 ± 0.3	S	14.7 ± 0.7	D, R
			14	2.0	19	1.2	17	4.8
SWIFT J2204.7+0337	IRAS 22017+0319	0.0611	9.8 ± 0.5	S	9.9 ± 2.7	S	32.4 ± 0.5	S
			16	0.9	17	0.2	20	8.4
SWIFT J2209.4−4711	NGC 7213	0.0058	$\leqslant 0.2$	S	$\leqslant 0.4$	S	1.8 ± 0.2	D, R
			18	1.0	21	1.3	16	2.6
SWIFT J2217.0+1413	Mrk 304	0.0704	$\leqslant 0.0$	S	0.3 ± 0.0	S	$\leqslant 0.0$	S
			17	1.1	17	1.3	22	4.7
SWIFT J2235.9−2602	NGC 7314	0.0048	16.5 ± 0.3	S	20.3 ± 0.1	S	69.9 ± 0.7	S
			16	1.6	18	1.2	18	3.9
SWIFT J2240.2+0801	UGC 12138	0.025	3.6 ± 0.2	S	3.7 ± 0.3	D, O	7.7 ± 0.6	S
			17	2.0	15	1.8	21	1.1
SWIFT J2254.1−1734	MR 2251−178	0.064	0.8 ± 0.1	S	$\leqslant 2.0$	S	7.3 ± 0.2	S
			16	2.3	20	3.1	19	2.8
SWIFT J2258.9+4054	UGC 12282	0.017	0.8 ± 0.1	S	$\leqslant 0.4$	S	2.3 ± 0.3	D, R
			17	5.0	19	0.8	16	1.3
SWIFT J2303.3+0852	NGC 7469	0.0163	15.7 ± 1.8	T, O+R	$\leqslant 11.0$	S	43.4 ± 6.5	T, O+R
			11	1.7	20	0.4	15	1.7
SWIFT J2304.8−0843	Mrk 926	0.0469	2.8 ± 0.2	S	2.8 ± 0.2	S	10.9 ± 0.4	S
			18	0.5	15	3.4	20	3.8
SWIFT J2304.9+1220	NGC 7479	0.0079	3.4 ± 0.5	S	2.7 ± 0.9	S	5.1 ± 0.5	D, R
			16	5.2	18	1.7	15	1.3
SWIFT J2318.4−4223	NGC 7582	0.0052	27.4 ± 1.7	D, R	45.2 ± 3.8	S	157.5 ± 7.1	D, R
			13	0.2	18	0.9	15	0.7
SWIFT J2318.9+0013	NGC 7603	0.0295	$\leqslant 0.4$	S	0.5 ± 0.1	S	2.8 ± 0.2	D, R
			18	1.0	18	2.2	18	1.7
SWIFT J2328.9+0328	NGC 7682	0.0171	2.1 ± 0.1	S	3.0 ± 0.1	S	13.5 ± 0.2	S
			16	3.3	17	3.0	20	7.1
SWIFT J2341.8+3033	UGC 12741	0.0174	0.5 ± 0.1	S	0.6 ± 0.1	S	2.3 ± 0.1	S
			16	2.9	18	2.1	20	4.6
SWIFT J2351.9−0109	PG 2349−014	0.174	0.7 ± 0.1	S	0.7 ± 0.1	S	3.3 ± 0.1	S
			17	0.6	20	1.3	19	1.6

Note. Flux values in units of 10−14 erg cm^{-2} s^{-1}. Table of Spitzer/IRS Fluxes. * For the Model column, "S," "D," and "T" indicate when a single, double, and triple Gaussian was used, respectively. Furthermore, "O" indicates when an additional Gaussian was included to account (with the exception of NGC 1068). Gaussian was included to reproduce a nearby emission line at longer (redder) wavelengths, "B" when an additional broad Gaussian line centered at the same wavelength as the expected emission line was included (with the exception of NGC 1068).

Table 5
Table of Spitzer/IRS Fluxes and Model Information for [S III] 18.7078 μm and [S III] 33.48 μm

SWIFT ID (1)	Source Name (2)	z (3)	[S III] 18.7078 μm (d.o.f) (4)	Model (χ^2) (5)	[S III] 33.48 μm (d.o.f) (6)	Model (χ^2) (7)
SWIFT J0006.2+2012	Mrk 335	0.0258	1.5 ± 0.4	S	1.9 ± 0.5	S
			16	4.7	13	1.9
SWIFT J0029.2+1319	PG 0026+129	0.142	⩽0.5	S	N/A	N/A
			16	1.5	N/A	N/A
SWIFT J0042.9−2332	NGC 235A	0.0222	4.4 ± 0.6	S	6.0 ± 1.0	S
			17	1.5	13	8.0
SWIFT J0048.8+3155	Mrk 348	0.015	8.0 ± 0.3	S	7.8 ± 0.4	S
			16	2.1	15	7.0
SWIFT J0059.4+3150	Mrk 352	0.0149	⩽0.1	S	N/A	N/A
			18	3.5	N/A	N/A
SWIFT J0111.4−3808	NGC 424	0.0118	7.8 ± 0.7	D, O	11.8 ± 0.1	S
			13	1.5	16	21.9
SWIFT J0114.4−5522	NGC 454	0.0121	1.5 ± 0.1	S	4.4 ± 0.2	S
			16	2.3	15	9.9
SWIFT J0123.8−3504	NGC 526A	0.0191	1.8 ± 0.5	S	4.5 ± 0.3	S
			17	3.9	15	13.2
SWIFT J0123.9−5846	Fairall 9	0.047	1.8 ± 0.2	S	1.5 ± 0.2	S
			12	3.8	13	10.9
SWIFT J0124.5+3350	NGC 513	0.0195	0.8 ± 0.1	S	8.9 ± 0.3	S
			16	3.8	14	9.1
SWIFT J0127.5+1910	Mrk 359	0.0174	2.7 ± 0.2	S	3.5 ± 0.4	S
			16	2.5	15	9.4
SWIFT J0138.6−4001	ESO 297−18	0.0252	1.4 ± 0.4	S	2.7 ± 0.1	S
			17	3.2	13	10.1
SWIFT J0152.8−0329	MCG −1−5−47	0.0172	0.5 ± 0.1	S	⩽0.8	S
			15	10.1	13	9.0
SWIFT J0201.0−0648	NGC 788	0.0136	4.6 ± 0.2	S	6.3 ± 0.1	S
			16	2.5	15	16.9
SWIFT J0214.6−0049	Mrk 590	0.0264	⩽0.1	S	6.7 ± 0.0	S
			18	3.8	14	14.8
SWIFT J0228.1+3118	Mrk 1040	0.0167	6.4 ± 0.9	D, O	18.4 ± 4.3	S
			13	1.3	15	31.6
SWIFT J0230.2−0900	Mrk 1044	0.0165	2.1 ± 0.1	S	4.1 ± 0.5	S
			16	1.1	14	20.5
SWIFT J0231.6−3645	IC 1816	0.017	6.7 ± 0.1	D, O	6.8 ± 0.1	S
			14	2.7	15	10.3
SWIFT J0234.1+3233	NGC 973	0.0162	3.8 ± 0.1	S	7.8 ± 0.6	S
			17	2.1	15	13.8
SWIFT J0234.6−0848	NGC 985	0.043	N/A	N/A	7.3 ± 0.4	S
			N/A	N/A	14	2.7
SWIFT J0238.2−5213	ESO 198−24	0.0455	0.5 ± 0.0	S	1.2 ± 0.0	S
			12	2.8	14	10.8
SWIFT J0241.3−0816	NGC 1052	0.005	4.2 ± 0.5	D, B	4.9 ± 0.2	S
			13	0.7	16	6.6
SWIFT J0242.6+0000	NGC 1068	0.0038	245.4 ± 34.4	S	163.5 ± 12.9	S
			16	3.4	16	6.6
SWIFT J0251.6−1639	NGC 1125	0.011	8.2 ± 0.3	S	28.6 ± 0.1	S
			16	1.7	16	21.6
SWIFT J0255.2−0011	NGC 1142	0.0289	0.4 ± 0.1	S	⩽1.5	S
			10	5.0	7	4.7
SWIFT J0256.4−3212	ESO 417−6	0.0163	1.3 ± 0.1	S	2.5 ± 0.3	S
			16	1.7	14	9.0
SWIFT J0304.1−0108	NGC 1194	0.0136	2.2 ± 0.4	S	⩽3.0	S
			16	1.5	17	10.7
SWIFT J0433.0+0521	3C 120	0.033	5.8 ± 0.3	S	17.4 ± 0.7	S
			15	5.1	13	6.3
SWIFT J0436.3−1022	Mrk 618	0.0355	3.2 ± 0.2	S	7.0 ± 0.3	S
			14	4.5	13	13.1
SWIFT J0451.4−0346	MCG −1−13−25	0.0159	0.8 ± 0.1	S	⩽1.4	S
			15	3.7	17	7.3
SWIFT J0456.3−7532	ESO 33−2	0.0181	3.2 ± 0.3	S	3.4 ± 0.3	S
			16	1.1	14	11.0

Table 5
(Continued)

SWIFT ID	Source Name	z	[S III] 18.7078 μm (d.o.f)	Model (χ^2)	[S III] 33.48 μm (d.o.f)	Model (χ^2)
(1)	(2)	(3)	(4)	(5)	(6)	(7)
SWIFT J0508.1+1727	2MASX J05081967+1721483	0.0175	4.0 ± 0.2 16	S 1.7	10.5 ± 0.1 15	S 5.8
SWIFT J0516.2−0009	Ark 120	0.0323	1.6 ± 0.2 16	S 2.9	6.4 ± 0.3 13	S 12.4
SWIFT J0501.9−3239	ESO 362−18	0.0125	1.9 ± 0.1 16	S 1.5	7.1 ± 0.3 16	S 7.3
SWIFT J0521.0−2522	IRAS 05189−2524	0.0426	N/A N/A	N/A N/A	8.3 ± 2.0 14	S 19.3
SWIFT J0552.2−0727	NGC 2110	0.0078	15.3 ± 0.5 16	S 2.9	29.6 ± 0.2 16	S 24.2
SWIFT J0557.9−3822	H0 557−385	0.0339	0.9 ± 0.1 14	S 8.3	1.5 ± 0.2 13	S 15.4
SWIFT J0601.9−8636	ESO 5−4	0.0062	2.1 ± 0.2 17	S 2.7	11.5 ± 2.2 16	S 5.4
SWIFT J0615.8+7101	Mrk 3	0.0135	52.4 ± 0.2 13	D, O 2.2	46.9 ± 4.1 12	D, B 2.5
SWIFT J0651.9+7426	Mrk 6	0.0188	14.7 ± 0.6 16	S 2.6	14.3 ± 0.9 14	S 8.9
SWIFT J0655.8+3957	UGC 3601	0.0171	4.1 ± 0.1 16	S 4.2	5.5 ± 0.4 14	S 13.6
SWIFT J0725.8+3000	Z 147−20	0.0188	1.4 ± 0.3 16	S 5.9	11.4 ± 0.8 14	S 5.3
SWIFT J0736.9+5846	Mrk 9	0.0399	$\leqslant$0.8 16	S 5.4	3.0 ± 0.1 14	S 3.2
SWIFT J0742.5+4948	Mrk 79	0.0222	8.3 ± 0.8 17	S 3.4	10.6 ± 0.3 13	S 4.5
SWIFT J0800.1+2638	IC 486	0.0269	3.0 ± 0.2 17	S 2.4	4.3 ± 0.0 13	S 9.2
SWIFT J0807.9+3859	Mrk 622	0.0232	3.7 ± 0.3 17	S 2.0	4.5 ± 0.5 13	S 3.8
SWIFT J0810.9+7602	PG 0804+761	0.1	1.0 ± 0.1 14	S 4.4	N/A N/A	N/A N/A
SWIFT J0856.0+7812	NGC 2655	0.0047	2.4 ± 0.3 16	S 2.8	4.0 ± 0.3 15	S 36.7
SWIFT J0902.0+6007	Mrk 18	0.0111	7.6 ± 0.2 16	S 3.7	17.7 ± 0.1 16	S 16.1
SWIFT J0918.5+1618	Mrk 704	0.0292	3.1 ± 0.5 17	S 4.2	2.2 ± 0.3 14	S 8.0
SWIFT J0920.8−0805	MCG −1−24−12	0.0196	2.0 ± 0.3 16	S 2.4	3.3 ± 0.4 14	S 11.1
SWIFT J0923.7+2255	Z 121−75	0.0323	2.6 ± 0.7 16	S 5.7	2.3 ± 0.6 13	S 8.6
SWIFT J0925.0+5218	Mrk 110	0.0353	0.8 ± 0.1 14	S 3.8	0.7 ± 0.1 11	S 4.7
SWIFT J0926.2+1244	Mrk 705	0.0291	2.0 ± 0.1 17	S 4.1	4.3 ± 0.0 14	S 5.5
SWIFT J0935.9+6120	UGC 5101	0.0394	N/A N/A	N/A N/A	12.0 ± 0.8 14	S 13.4
SWIFT J0945.6−1420	NGC 2992	0.0077	23.9 ± 0.5 16	S 3.0	44.5 ± 1.5 17	S 20.9
SWIFT J0947.6−3057	MCG −5−23−16	0.0085	4.2 ± 0.6 17	S 1.6	9.7 ± 1.2 16	S 14.7
SWIFT J0959.5−2248	NGC 3081	0.008	12.2 ± 0.4 16	S 4.1	16.5 ± 0.2 16	S 10.0
SWIFT J1001.8+2848	3C 234	0.1849	$\leqslant$1.1 17	S 5.3	N/A N/A	N/A N/A
SWIFT J1001.7+5543	NGC 3079	0.0037	4.3 ± 0.3 16	S 1.1	43.8 ± 1.3 16	S 9.9
SWIFT J1023.5+1952	NGC 3227	0.0039	21.2 ± 0.6 16	S 1.0	24.4 ± 0.9 16	S 28.8
SWIFT J1031.7−3451	NGC 3281	0.0107	15.5 ± 0.6 16	S 1.6	26.8 ± 0.4 16	S 10.2

Table 5
(Continued)

SWIFT ID (1)	Source Name (2)	z (3)	[S III] 18.7078 μm (d.o.f) (4)	Model (χ^2) (5)	[S III] 33.48 μm (d.o.f) (6)	Model (χ^2) (7)
SWIFT J1048.4−2511	NGC 3393	0.0125	32.0 ± 0.5	S	40.9 ± 0.0	S
			16	6.9	16	7.7
SWIFT J1106.5+7234	NGC 3516	0.0088	3.5 ± 0.3	S	6.3 ± 0.6	S
			16	3.6	16	17.4
SWIFT J1139.0−3743	NGC 3783	0.0097	7.9 ± 0.8	S	4.5 ± 0.6	S
			16	5.3	17	9.0
SWIFT J1139.8+3157	NGC 3786	0.0089	6.8 ± 0.2	S	12.3 ± 0.3	S
			16	3.3	17	11.0
SWIFT J1143.7+7942	UGC 6728	0.0065	0.6 ± 0.1	S	2.2 ± 0.7	S
			16	2.8	14	4.7
SWIFT J1157.8+5529	NGC 3998	0.0035	2.0 ± 0.1	S	1.7 ± 0.1	S
			16	1.1	16	12.1
SWIFT J1203.0+4433	NGC 4051	0.0023	7.4 ± 0.4	S	9.6 ± 0.4	S
			16	1.1	16	6.5
SWIFT J1204.9+3105	UGC 7064	0.025	3.4 ± 0.2	S	5.3 ± 0.0	S
			16	1.8	13	15.8
SWIFT J1206.2+5243	NGC 4102	0.0028	73.9 ± 1.5	S	113.2 ± 4.7	S
			16	0.8	16	7.9
SWIFT J1209.4+4340	NGC 4138	0.003	0.6 ± 0.1	S	⩽0.5	S
			16	2.5	12	6.7
SWIFT J1210.5+3924	NGC 4151	0.0033	70.4 ± 1.5	S	46.0 ± 0.9	S
			16	4.0	16	16.6
SWIFT J1218.5+2952	NGC 4253	0.0129	11.3 ± 0.4	S	16.7 ± 0.9	S
			16	1.6	15	35.6
SWIFT J1219.4+4720	NGC 4258	0.0017	1.6 ± 0.2	S	5.5 ± 0.2	S
			16	1.7	16	9.7
SWIFT J1225.8+1240	NGC 4388	0.0084	31.9 ± 0.8	S	56.9 ± 2.5	S
			16	4.6	17	26.2
SWIFT J1202.5+3332	NGC 4395	0.0011	2.4 ± 0.1	S	3.0 ± 0.2	S
			15	1.6	16	7.9
SWIFT J1229.1+0202	3C 273	0.1583	1.1 ± 0.3	S	N/A	N/A
			15	1.0	N/A	N/A
SWIFT J1232.1+2009	Mrk 771	0.063	1.2 ± 0.3	S	1.0 ± 0.2	S
			15	1.2	15	4.9
SWIFT J1235.6−3954	NGC 4507	0.0118	14.3 ± 0.5	S	15.3 ± 0.0	S
			16	3.9	16	21.3
SWIFT J1238.6+0928	SDSS J123843.43+092736.6	0.0829	0.8 ± 0.3	S	1.6 ± 0.1	S
			14	3.7	15	9.5
SWIFT J1239.6−0519	NGC 4593	0.009	2.9 ± 0.2	S	5.8 ± 0.4	S
			16	1.4	17	7.4
SWIFT J1246.6+5435	NGC 4686	0.0167	0.4 ± 0.0	S	⩽1.8	S
			16	3.9	14	9.1
SWIFT J1252.3−1323	NGC 4748	0.0146	3.9 ± 0.3	S	18.0 ± 0.2	S
			17	1.3	15	11.7
SWIFT J1300.1+1635	SDSS J130005.35+163214.8	0.08	N/A	N/A	N/A	N/A
			N/A	N/A	N/A	N/A
SWIFT J1304.3−0532	NGC 4941	0.004	7.9 ± 0.2	S	4.8 ± 0.6	S
			16	3.8	16	5.8
SWIFT J1304.3−1022	NGC 4939	0.0104	10.8 ± 0.1	S	11.8 ± 0.0	S
			16	4.0	15	13.7
SWIFT J1305.4−4928	NGC 4945	0.0019	16.3 ± 0.4	S	293.7 ± 11.1	S
			16	0.6	16	6.1
SWIFT J1306.4−4025A	ESO 323−77	0.015	10.5 ± 0.5	S	34.8 ± 1.5	S
			16	1.1	15	24.8
SWIFT J1322.2−1641	MCG −3−34−64	0.0165	27.9 ± 5.7	D, B	32.4 ± 1.6	S
			13	2.9	14	20.3
SWIFT J1325.4−4301	Cen A	0.0018	36.5 ± 0.6	S	91.7 ± 2.6	S
			16	2.1	16	16.5
SWIFT J1335.8−3416	MCG −6−30−15	0.0077	3.8 ± 0.3	S	4.7 ± 0.1	S
			16	3.4	17	5.3
SWIFT J1341.9+3537	NGC 5273	0.0035	2.1 ± 0.3	S	⩽0.6	S
			16	3.5	18	12.2

Table 5
(Continued)

SWIFT ID (1)	Source Name (2)	z (3)	[S III] 18.7078 μm (d.o.f) (4)	Model (χ^2) (5)	[S III] 33.48 μm (d.o.f) (6)	Model (χ^2) (7)
SWIFT J1349.3−3018	IC 4329A	0.016	18.7 ± 0.9 17	S 3.3	31.6 ± 1.8 15	S 13.6
SWIFT J1352.8+6917	Mrk 279	0.0304	4.7 ± 0.3 17	S 3.1	4.9 ± 0.3 13	S 4.0
SWIFT J1355.9+1822	Mrk 463	0.0504	11.0 ± 0.5 14	S 4.7	11.1 ± 0.5 13	S 1.4
SWIFT J1413.2−0312	NGC 5506	0.0062	65.0 ± 14.1 14	D, B 1.5	79.4 ± 2.4 16	S 15.5
SWIFT J1417.9+2507	NGC 5548	0.0172	3.4 ± 0.3 16	S 2.5	4.2 ± 0.1 14	S 9.4
SWIFT J1429.2+0118	Mrk 1383	0.0865	0.8 ± 0.3 14	S 0.7	2.4 ± 0.0 14	S 14.0
SWIFT J1432.8−4412	NGC 5643	0.004	19.2 ± 0.6 16	S 2.1	16.5 ± 1.1 16	S 15.4
SWIFT J1433.9+0528	NGC 5674	0.0249	3.2 ± 0.0 16	S 3.6	5.7 ± 0.0 13	S 5.0
SWIFT J1436.4+5846	Mrk 817	0.0314	1.7 ± 0.3 17	S 3.5	4.0 ± 0.9 13	S 9.6
SWIFT J1442.5−1715	NGC 5728	0.0093	14.9 ± 0.4 17	S 2.2	28.6 ± 0.3 16	S 25.8
SWIFT J1457.8−4308	IC 4518A	0.0163	16.9 ± 0.3 16	S 1.7	36.4 ± 1.8 15	S 25.3
SWIFT J1504.2+1025	Mrk 841	0.0364	4.1 ± 0.3 13	S 1.7	4.2 ± 0.0 14	S 9.0
SWIFT J1512.0−2119	IRAS 15091−2107	0.0446	9.9 ± 0.4 13	S 6.2	13.0 ± 0.4 14	S 20.5
SWIFT J1515.0+4205	NGC 5899	0.0086	4.9 ± 0.3 16	S 5.4	10.8 ± 0.1 10	S 6.7
SWIFT J1548.5−1344	NGC 5995	0.0252	5.8 ± 0.5 17	S 5.0	10.7 ± 0.6 13	S 4.4
SWIFT J1628.1+5145	Mrk 1498	0.0547	1.7 ± 0.0 16	S 5.4	4.0 ± 0.6 10	D, O 20.2
SWIFT J1652.0−5915B	NGC 6221	0.005	83.4 ± 1.7 16	S 3.6	172.1 ± 10.6 16	S 13.6
SWIFT J1652.9+0223	NGC 6240	0.0245	16.2 ± 0.8 17	S 5.0	80.4 ± 6.1 13	S 18.9
SWIFT J1717.1−6249	NGC 6300	0.0037	5.2 ± 0.4 16	S 1.5	5.1 ± 0.9 16	S 5.1
SWIFT J1822.0+6421	Q 1821+643	0.297	3.8 ± 0.3 14	S 2.4	N/A N/A	N/A N/A
SWIFT J1836.9−5924	Fairall 49	0.0202	10.1 ± 0.6 16	S 4.0	21.8 ± 1.0 14	S 7.2
SWIFT J1838.4−6524	ESO 103−35	0.0133	8.7 ± 0.6 16	S 0.9	24.3 ± 1.6 18	S 16.0
SWIFT J1842.0+7945	3C 390.3	0.0561	1.0 ± 0.2 16	S 1.9	1.3 ± 0.2 15	S 31.0
SWIFT J1844.5−6221	Fairall 51	0.0142	8.0 ± 0.3 16	S 0.9	13.5 ± 0.9 16	S 11.1
SWIFT J1848.0−7832	LEDA 89032	0.0741	0.7 ± 0.2 14	S 2.4	⩽0.8 17	S 12.1
SWIFT J1921.1−5842	ESO 141−55	0.036	⩽0.0 16	S 5.0	2.9 ± 0.2 14	S 5.5
SWIFT J1942.6−1024	NGC 6814	0.0058	5.9 ± 0.3 16	S 3.4	3.4 ± 1.0 16	S 9.5
SWIFT J2009.0−6103	NGC 6860	0.0149	3.1 ± 0.1 16	S 1.3	5.2 ± 0.0 16	S 6.5
SWIFT J2042.3+7507	4C +74.26	0.104	⩽0.4 18	S 1.2	N/A N/A	N/A N/A
SWIFT J2044.2−1045	Mrk 509	0.0344	5.8 ± 0.4 14	S 5.0	10.9 ± 0.5 13	S 9.5
SWIFT J2052.0−5704	IC 5063	0.0114	17.9 ± 0.9 16	S 6.0	29.1 ± 0.0 16	S 24.9

Table 5
(Continued)

SWIFT ID (1)	Source Name (2)	z (3)	[S III] 18.7078 μm (d.o.f) (4)	Model (χ^2) (5)	[S III] 33.48 μm (d.o.f) (6)	Model (χ^2) (7)
SWIFT J2148.3−3454	NGC 7130	0.0162	17.6 ± 0.5	S	50.2 ± 0.8	S
			16	5.0	15	26.0
SWIFT J2204.7+0337	IRAS 22017+0319	0.0611	5.0 ± 0.5	S	4.1 ± 0.9	S
			16	1.3	14	6.5
SWIFT J2209.4−4711	NGC 7213	0.0058	3.5 ± 0.3	S	3.2 ± 0.5	S
			16	2.0	16	9.6
SWIFT J2217.0+1413	Mrk 304	0.0704	$\leqslant$0.0	S	$\leqslant$0.4	S
			17	5.0	17	5.1
SWIFT J2235.9−2602	NGC 7314	0.0048	8.7 ± 0.3	S	11.0 ± 0.5	S
			16	1.3	16	11.0
SWIFT J2240.2+0801	UGC 12138	0.025	1.9 ± 0.3	S	3.0 ± 0.2	S
			16	3.0	13	12.7
SWIFT J2254.1−1734	MR 2251−178	0.064	1.1 ± 0.2	S	$\leqslant$2.2	S
			16	5.1	16	20.6
SWIFT J2258.9+4054	UGC 12282	0.017	0.3 ± 0.1	S	3.2 ± 0.7	S
			17	4.0	15	8.7
SWIFT J2303.3+0852	NGC 7469	0.0163	65.3 ± 1.2	S	104.6 ± 6.1	S
			16	4.8	15	5.8
SWIFT J2304.8−0843	Mrk 926	0.0469	4.3 ± 0.7	S	5.0 ± 0.3	S
			11	2.5	14	22.1
SWIFT J2304.9+1220	NGC 7479	0.0079	2.1 ± 0.7	S	$\leqslant$2.3	S
			16	3.7	18	24.1
SWIFT J2318.4−4223	NGC 7582	0.0052	68.3 ± 2.8	S	144.8 ± 10.5	S
			16	0.9	16	7.4
SWIFT J2318.9+0013	NGC 7603	0.0295	3.3 ± 0.5	S	7.9 ± 0.2	S
			16	6.8	13	7.1
SWIFT J2328.9+0328	NGC 7682	0.0171	3.4 ± 0.1	S	4.6 ± 0.3	S
			15	6.5	15	11.8
SWIFT J2341.8+3033	UGC 12741	0.0174	0.5 ± 0.0	S	2.5 ± 0.3	S
			16	7.8	13	7.0
SWIFT J2351.9−0109	PG 2349−014	0.174	1.0 ± 0.1	S	N/A	N/A
			16	1.4	N/A	N/A

Note. Flux values in units of 10−14 erg cm^{-2} s^{-1}. Table of Spitzer/IRS fluxes. *The representations for this table resemble those of Table 4.

Table 6
List of Upper Limits Calculated for all MIR Lines and Corresponding SWIFT IDs

[Ne V] 14.32 μm	[S III] 18.71 μm	[Ne V] 24.32 μm	[O IV] 25.89 μm	[S III] 33.48 μm
SWIFT J0059.4+3150	SWIFT J0029.2+1319	SWIFT J0029.2+1319	SWIFT J0255.2−0011	SWIFT J0152.8−0329
SWIFT J0124.5+3350	SWIFT J0059.4+3150	SWIFT J0059.4+3150	SWIFT J1206.2+5243	SWIFT J0255.2−0011
SWIFT J0230.2−0900	SWIFT J0214.6−0049	SWIFT J0138.6−4001	SWIFT J1305.4−4928	SWIFT J0304.1−0108
SWIFT J0238.2−5213	SWIFT J0736.9+5846	SWIFT J0152.8−0329	SWIFT J2217.0+1413	SWIFT J0451.4−0346
SWIFT J0241.3−0816	SWIFT J1001.8+2848	SWIFT J0241.3−0816		SWIFT J1209.4+4340
SWIFT J0255.2−0011	SWIFT J1921.1−5842	SWIFT J0255.2−0011		SWIFT J1246.6+5435
SWIFT J0451.4−0346	SWIFT J2042.3+7507	SWIFT J0508.1+1727		SWIFT J1341.9+3537
SWIFT J0601.9−8636	SWIFT J2217.0+1413	SWIFT J0601.9−8636		SWIFT J1848.0−7832
SWIFT J0725.8+3000		SWIFT J0725.8+3000		SWIFT J2217.0+1413
SWIFT J0810.9+7602		SWIFT J0807.9+3859		SWIFT J2254.1−1734
SWIFT J1219.4+4720		SWIFT J1157.8+5529		SWIFT J2304.9+1220
SWIFT J1229.1+0202		SWIFT J1206.2+5243		
SWIFT J1305.4−4928		SWIFT J1219.4+4720		
SWIFT J2042.3+7507		SWIFT J1305.4−4928		
SWIFT J2209.4−4711		SWIFT J1436.4+5846		
SWIFT J2217.0+1413		SWIFT J1652.0−5915B		
SWIFT J2318.9+0013		SWIFT J1652.9+0223		
		SWIFT J2209.4−4711		
		SWIFT J2254.1−1734		
		SWIFT J2258.9+4054		
		SWIFT J2303.3+0852		

Note. See Section 3.2 for further details

Appendix C
Best-fit Centroid Wavelength

In Figure 9, we show the histograms of the best-fit centroid wavelengths for the [Ne V] 14.32/24.32 μm, [O IV] 25.89 μm, and [S III] 18.71/33.48 μm lines. We also illustrate, as dotted vertical lines, the expected centroid wavelength of the lines, showing that the vast majority of the lines are found at wavelengths consistent with the expected ones.

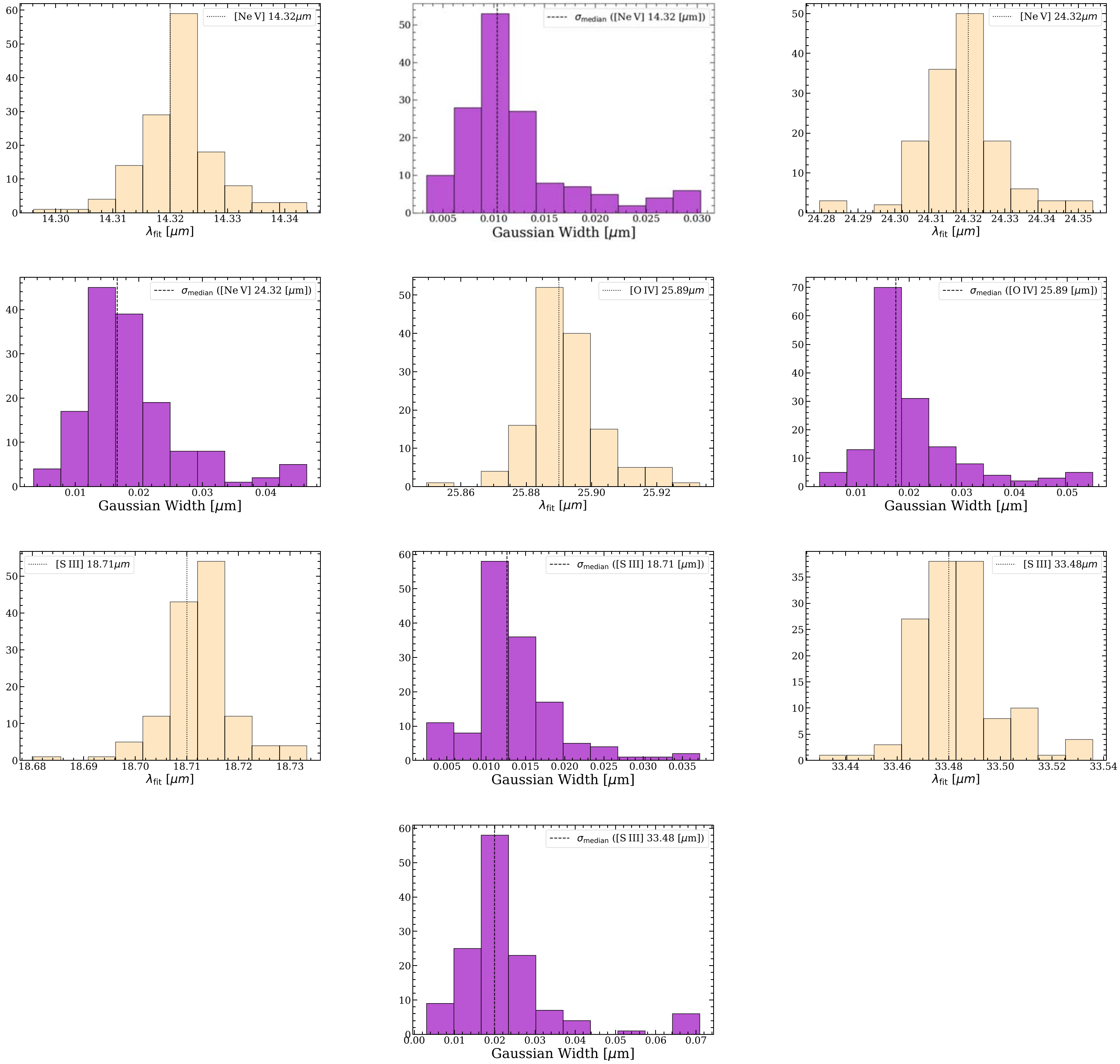

Figure 9. Left panels: histograms of the best-fit, λ_{fit}, centroid wavelength from the line fitting method (see Section 3) for the forbidden emission lines [Ne V] 14.32/24.32 μm, [S III] 18.71/33.48 μm, and [O IV] 25.89 μm. The distribution of wavelength peaks at the expected wavelength for all five lines (dotted vertical lines). Right panels: histograms of the characteristic width of the Gaussian fits for the five MIR lines. If a source was considered to contain a blueshifted line and/or a broad emission line, where the second/third Gaussian flux was included in the total reported flux (see Sections 3.3.2, 3.3.3, and 3.3.4), then the corresponding σ was included as an additional data point in the histogram.

Appendix D
Comparison with Weaver et al. 2010

In Figure 10, we compare the logs of [Ne V] 14.32/24.32 μm and [O IV] 25.89 μm fluxes we obtained with the log of those reported by K. A. Weaver et al. (2010). K. A. Weaver et al. (2010) studied Spitzer spectra for a sample of 79 hard X-ray selected AGN from earlier versions of the Swift/BAT catalog (J. Tueller et al. 2008, 2010). About half of the sources (75) of our sample overlap with K. A. Weaver et al. (2010). For those sources, our log(fluxes) agree very well with those of K. A. Weaver et al. (2010), showing very little scatter (0.02, 0.03, and 0.04 dex for [Ne V] 14.32/24.32 μm and [O IV] 25.89 μm, respectively).

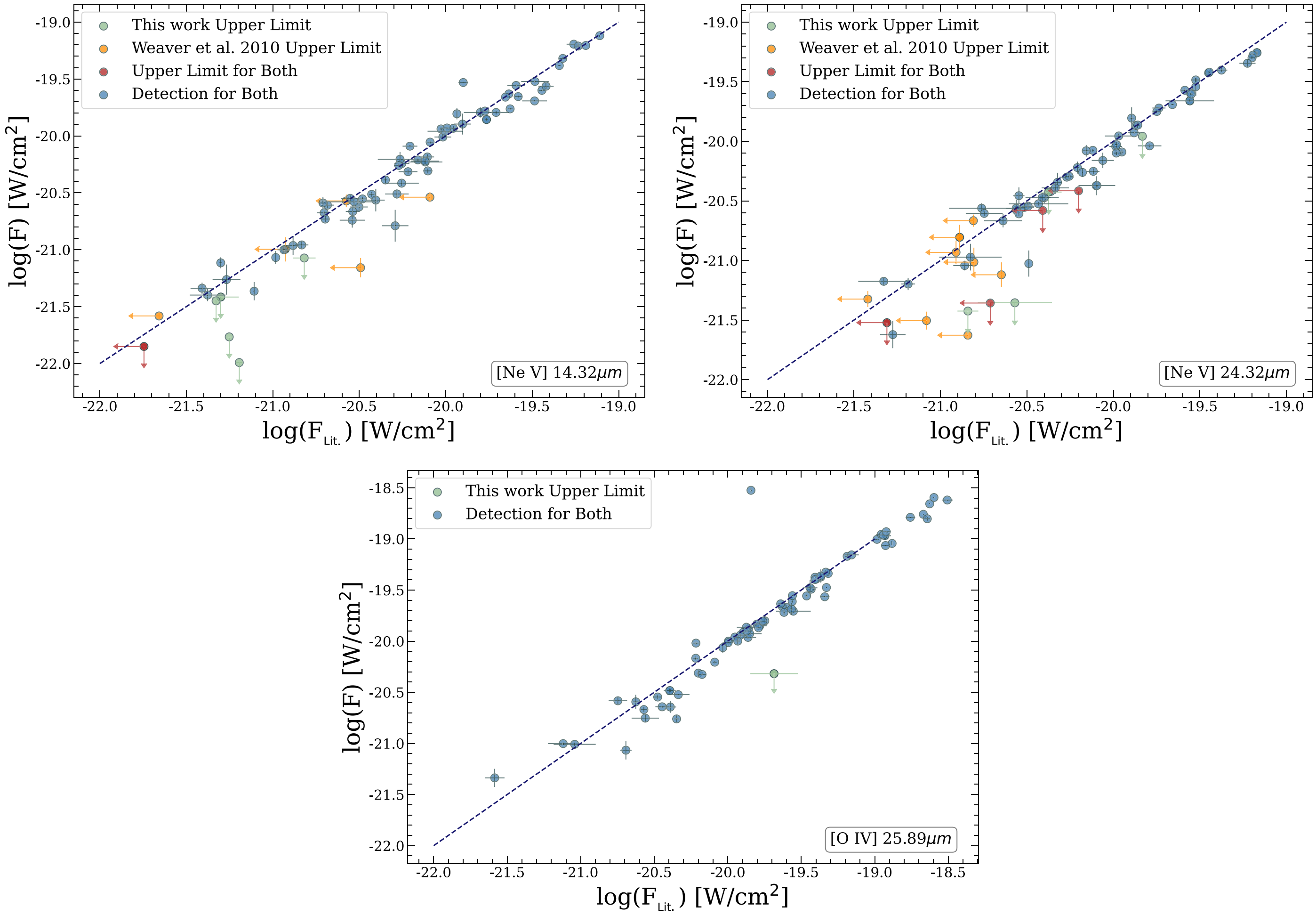

Figure 10. For the 75 sources from K. A. Weaver et al. (2010) that are also in our sample, we compare the log of their emission line fluxes with the log of our measurements for the [Ne V] 14.32, [Ne V] 24.32, and [O IV] 25.89 μm lines in the top left, top right and bottom panels, respectively. Objects shown in blue have 3σ detections in both works; those in orange and red have upper limits. The dashed line shows the 1:1 relationship; our measurements are consistent with those of K. A. Weaver et al. (2010). Objects for which only upper limits are derived have low signal-to-noise spectra, but even for these fainter objects, our measurements are still in agreement. We therefore believe our results are consistent with K. A. Weaver et al. (2010), but we make use of a much larger sample of AGN with Spitzer spectra and so we perform our own emission line measurements in a consistent manner across our whole sample. Note: the values in K. A. Weaver et al. (2010) were reported in units of watts per square centimeter. As such, we converted our units to match theirs, but only for this comparison.

ORCID iDs

C. Ricci https://orcid.org/0000-0001-5231-2645
M. J. Temple https://orcid.org/0000-0001-8433-550X
S. Satyapal https://orcid.org/0000-0003-2277-2354
J. Cann https://orcid.org/0000-0003-1051-6564
Y. Xie https://orcid.org/0000-0002-9707-1037
Y. Diaz https://orcid.org/0000-0002-8604-1158
K. Ichikawa https://orcid.org/0000-0002-4377-903X
M. J. Koss https://orcid.org/0000-0002-7998-9581
F. E. Bauer https://orcid.org/0000-0002-8686-8737
A. Rojas https://orcid.org/0000-0003-0006-8681
D. Kakkad https://orcid.org/0000-0002-2603-2639
A. Tortosa https://orcid.org/0000-0003-3450-6483
F. Ricci https://orcid.org/0000-0001-5742-5980
R. Mushotzky https://orcid.org/0000-0002-7962-5446
T. Kawamuro https://orcid.org/0000-0002-6808-2052
K. K. Gupta https://orcid.org/0009-0007-9018-1077
B. Trakhtenbrot https://orcid.org/0000-0002-3683-7297
C. S. Chang https://orcid.org/0000-0001-9910-3234
R. Riffel https://orcid.org/0000-0002-1321-1320
K. Oh https://orcid.org/0000-0002-5037-951X
F. Harrison https://orcid.org/0000-0002-4226-8959
M. Powell https://orcid.org/0000-0003-2284-8603
D. Stern https://orcid.org/0000-0003-2686-9241
C. M. Urry https://orcid.org/0000-0002-0745-9792

References

Abel, N. P., & Satyapal, S. 2008, ApJ, 678, 686
Almeida, C. R., & Ricci, C. 2017, NatAs, 1, 679
Antonucci, R. 1993, ARA&A, 31, 473
Armus, L., Bernard-Salas, J., Spoon, H. W. W., et al. 2006, ApJ, 640, 204
Asmus, D., Gandhi, P., Honig, S. F., Smette, A., & Duschl, W. J. 2015, MNRAS, 454, 766
Assef, R. J., Eisenhardt, P. R. M., Stern, D., et al. 2015, ApJ, 804, 27
Baek, J., Chung, A., Schawinski, K., et al. 2019, MNRAS, 488, 4317
Baldwin, J. A., Phillips, M. M., & Terlevich, R. 1981, PASP, 93, 5
Barthelmy, S. D., Barbier, L. M., Cummings, J. R., et al. 2005, SSRv, 120, 143
Bassani, L., Dadina, M., Maiolino, R., et al. 1999, ApJS, 121, 473
Baumgartner, W. H., Tueller, J., Markwardt, C. B., et al. 2013, ApJS, 207, 19
Berney, S., Koss, M., Trakhtenbrot, B., et al. 2015, MNRAS, 454, 3622
Bischetti, M., Piconcelli, E., Vietri, G., et al. 2017, A&A, 598, A122
Burlon, D., Ajello, M., Greiner, J., et al. 2011, ApJ, 728, 58
Cameron, E. 2011, PASA, 28, 128
Cann, J. M., Satyapal, S., Abel, N. P., et al. 2018, ApJ, 861, 142
Cerqueira-Campos, F. C., Rodriguez-Ardila, A., Panda, S., et al. 2023, MNRAS, 524, 542
Cerqueira-Campos, F. C., Rodriguez-Ardila, A., Riffel, R., et al. 2021, MNRAS, 500, 2666
Curran, P. A. 2014, arXiv:1411.3816
den Brok, J. S., Koss, M. J., Trakhtenbrot, B., et al. 2022, ApJS, 261, 7
Díaz-Santos, T., Assef, R. J., Blain, A. W., et al. 2016, ApJ, 816, L6
Elvis, M., Wilkes, B. J., McDowell, J. C., et al. 1994, ApJS, 95, 1
Feltre, A., Gruppioni, C., Marchetti, L., et al. 2023, A&A, 675, A74
Fonseca-Faria, M. A., Rodriguez-Ardila, A., Contini, M., & Reynaldi, V. 2021, MNRAS, 506, 3831
Gandhi, P., Horst, H., Smette, A., et al. 2009, A&A, 502, 457
Gardner, J. P., Mather, J. C., Clampin, M., et al. 2006, SSRv, 123, 485
Gebhardt, K., Bender, R., Bower, G., et al. 2000, ApJL, 539, L13
Gehrels, N., Chincarini, G., Giommi, P., et al. 2004, ApJ, 611, 1005
Goulding, A. D., & Alexander, D. M. 2009, MNRAS, 398, 1165
Gruppioni, C., Berta, S., Spinoglio, L., et al. 2016, MNRAS, 458, 4297
Gupta, K. K., Ricci, C., Temple, M. J., et al. 2024, A&A, 691, A203
Hermosa Muñoz, L., Alonso-Herrero, A., Pereira-Santaella, M., et al. 2024, A&A, 690, A350
Hickox, R. C., & Alexander, D. M. 2018, ARA&A, 56, 625
Ho, L. C. 2008, ARA&A, 46, 475
Ichikawa, K., Ricci, C., Ueda, Y., et al. 2017, ApJ, 835, 74
Ichikawa, K., Ricci, C., Ueda, Y., et al. 2019, ApJ, 870, 31
Izotov, Y. I., Thuan, T. X., & Privon, G. 2012, MNRAS, 427, 1229
Jarrett, T. H., Chester, T., Cutri, R., et al. 2000, AJ, 119, 2498
Kakkad, D., Sani, E., Rojas, A. F., et al. 2022, MNRAS, 511, 2105
Kauffmann, G., Heckman, T. M., Tremonti, C., et al. 2003, MNRAS, 346, 1055
Kawamuro, T., Ricci, C., Imanishi, M., et al. 2022, ApJ, 938, 87
Kawamuro, T., Ricci, C., Mushotzky, R. F., et al. 2023, ApJS, 269, 24
Kewley, L. J., Dopita, M. A., Sutherland, R. S., Heisler, C. A., & Trevena, J. 2001, ApJ, 556, 121
Kormendy, J., & Ho, L. C. 2013, ARA&A, 51, 511
Kormendy, J., & Richstone, D. 1995, ARA&A, 33, 581
Koss, M., Mushotzky, R., Veilleux, S., et al. 2011, ApJ, 739, 57
Koss, M., Trakhtenbrot, B., Ricci, C., et al. 2017, ApJ, 850, 74
Koss, M. J., Blecha, L., Bernhard, P., et al. 2018, Nature, 563, 214
Koss, M. J., Ricci, C., Trakhtenbrot, B., et al. 2022a, ApJS, 261, 2
Koss, M. J., Strittmatter, B., Lamperti, I., et al. 2021, ApJS, 252, 29
Koss, M. J., Trakhtenbrot, B., Ricci, C., et al. 2022b, ApJS, 261, 1
Koss, M. J., Trakhtenbrot, B., Ricci, C., et al. 2022c, ApJS, 261, 6
Lamperti, I., Koss, M., Trakhtenbrot, B., et al. 2017, MNRAS, 467, 540
Lebouteiller, V., Barry, D. J., Goes, C., et al. 2015, ApJS, 218, 21
Liu, T., Wang, J.-X., Yang, H., Zhu, F.-F., & Zhou, Y.-Y. 2014, ApJ, 783, 106
Lusso, E., Comastri, A., Simmons, B. D., et al. 2012, MNRAS, 425, 623
Maddox, N. 2018, MNRAS, 480, 5203
Magorrian, J., Tremaine, S., Richstone, D., et al. 1998, AJ, 115, 2285
Martocchia, S., Piconcelli, E., Zappacosta, L., et al. 2017, A&A, 608, A51
Mazzalay, X., Rodriguez-Ardila, A., Komossa, S., & McGregor, P. J. 2013, MNRAS, 430, 2411
McKaig, J. D., Satyapal, S., Laor, A., et al. 2024, arXiv:2408.15229
Mejía-Restrepo, J. E., Trakhtenbrot, B., Koss, M. J., et al. 2022, ApJS, 261, 5
Meléndez, M., Kraemer, S. B., Armentrout, B. K., et al. 2008, ApJ, 682, 94
Mullaney, J. R., Alexander, D. M., Goulding, A. D., & Hickox, R. C. 2011, MNRAS, 414, 1082
Negus, J., Comerford, J. M., Müller Sánchez, F., et al. 2021, ApJ, 920, 62
Negus, J., Comerford, J. M., Sánchez, F. M., et al. 2023, ApJ, 945, 127
Netzer, H. 2015, ARA&A, 53, 365
Newville, M., Stensitzki, T., Allen, D. B., & Ingargiola, A. 2014, LMFIT: Non-Linear Least-Square Minimization and Curve-Fitting for Python, 0.8.0, Zenodo, doi:10.5281/zenodo.11813
Oh, K., Koss, M. J., Ueda, Y., et al. 2022, ApJS, 261, 4
Oh, K., Schawinski, K., Koss, M., et al. 2017, MNRAS, 464, 1466
Pereira-Santaella, M., Diamond-Stanic, A. M., Alonso-Herrero, A., & Rieke, G. H. 2010, ApJ, 725, 2270
Perna, M., Lanzuisi, G., Brusa, M., Mignoli, M., & Cresci, G. 2017, A&A, 603, A99
Privon, G. C., Ricci, C., Aalto, S., et al. 2020, ApJ, 893, 149
Ricci, C., Ananna, T. T., Temple, M. J., et al. 2022a, ApJ, 938, 67
Ricci, C., Bauer, F. E., Treister, E., et al. 2017a, MNRAS, 468, 1273
Ricci, C., Chang, C.-S., Kawamuro, T., et al. 2023, ApJL, 952, L28
Ricci, C., Ho, L. C., Fabian, A. C., et al. 2018, MNRAS, 480, 1819
Ricci, C., Privon, G. C., Pfeifle, R. W., et al. 2021, MNRAS, 506, 5935
Ricci, C., Trakhtenbrot, B., Koss, M. J., et al. 2017b, ApJS, 233, 17
Ricci, C., Trakhtenbrot, B., Koss, M. J., et al. 2017c, Nature, 549, 488
Ricci, C., Ueda, Y., Koss, M. J., et al. 2015, ApJL, 815, L13
Ricci, F., Treister, E., Bauer, F. E., et al. 2022b, ApJS, 261, 8
Rodríguez-Ardila, A., & Fonseca-Faria, M. A. 2020, ApJL, 895, L9
Rodríguez-Ardila, A., Mason, R. E., Martins, L., et al. 2017, MNRAS, 465, 906
Rojas, A. F., Sani, E., Gavignaud, I., et al. 2020, MNRAS, 491, 5867
Satyapal, S., Böker, T., Mcalpine, W., et al. 2009, ApJ, 704, 439
Satyapal, S., Kamal, L., Cann, J. M., Secrest, N. J., & Abel, N. P. 2021, ApJ, 906, 35
Satyapal, S., Vega, D., Dudik, R. P., Abel, N. P., & Heckman, T. 2008, ApJ, 677, 926
Satyapal, S., Vega, D., Heckman, T., O'Halloran, B., & Dudik, R. 2007, ApJL, 663, L9
Shen, Y. 2013, BASI, 41, 61
Smith, K. L., Mushotzky, R. F., Koss, M., et al. 2020, MNRAS, 492, 4216
Spinoglio, L., Fernández-Ontiveros, J. A., & Malkan, M. A. 2022, ApJ, 941, 46
Sturm, E., Lutz, D., Verma, A., et al. 2002, A&A, 393, 821
Tanimoto, A., Ueda, Y., Odaka, H., Yamada, S., & Ricci, C. 2022, ApJS, 260, 30
Tommasin, S., Spinoglio, L., Malkan, M. A., & Fazio, G. 2010, ApJ, 709, 1257
Tommasin, S., Spinoglio, L., Malkan, M. A., et al. 2008, ApJ, 676, 836
Torres-Albà, N., Marchesi, S., Zhao, X., et al. 2021, ApJ, 922, 252
Trakhtenbrot, B., Ricci, C., Koss, M. J., et al. 2017, MNRAS, 470, 800
Tueller, J., Baumgartner, W. H., Markwardt, C. B., et al. 2010, ApJS, 186, 378
Tueller, J., Mushotzky, R. F., Barthelmy, S., et al. 2008, ApJ, 681, 113

Ueda, Y., Hashimoto, Y., Ichikawa, K., et al. 2015, ApJ, 815, 1
Urry, C. M., & Padovani, P. 1995, PASP, 107, 803
Vasudevan, R. V., & Fabian, A. C. 2009, MNRAS, 392, 1124
Veilleux, S., & Osterbrock, D. E. 1987, ApJS, 63, 295
Weaver, K. A., Meléndez, M., Mushotzky, R. F., et al. 2010, ApJ, 716, 1151
Weedman, D. W., Hao, L., Higdon, S. J. U., et al. 2005, ApJ, 633, 706
Yamada, S., Ueda, Y., Kawamuro, T., et al. 2024, ApJ, 965, 153
Yamada, S., Ueda, Y., Tanimoto, A., et al. 2021, ApJS, 257, 61
Zappacosta, L., Piconcelli, E., Giustini, M., et al. 2020, A&A, 635, L5
Zhang, L., Packham, C., Hicks, E. K. S., et al. 2024, ApJ, 974, 195